

## EMISSION LINE PROPERTIES OF THE LARGE BRIGHT QUASAR SURVEY

KARL FORSTER,

email: [kforster@cfa.harvard.edu](mailto:kforster@cfa.harvard.edu)

PAUL J. GREEN, THOMAS L. ALDCROFT,

Harvard-Smithsonian Center for Astrophysics, 60 Garden St., Cambridge, MA 02138

email: [pgreen@cfa.harvard.edu](mailto:pgreen@cfa.harvard.edu), [aldcroft@cfa.harvard.edu](mailto:aldcroft@cfa.harvard.edu)

MARIANNE VESTERGAARD

The Ohio State University, 140 West 18th Avenue, Columbus, OH 43210-1173

email: [vester@astronomy.ohio-state.edu](mailto:vester@astronomy.ohio-state.edu)

CRAIG B. FOLTZ

Multiple Mirror Telescope Observatory, University of Arizona, Tucson, AZ 85721

email: [cfoltz@as.arizona.edu](mailto:cfoltz@as.arizona.edu)

AND

PAUL C. HEWETT

Institute of Astronomy, Madingley Road, Cambridge, CB3 0HA, UK

email: [phewett@ast.cam.ac.uk](mailto:phewett@ast.cam.ac.uk)

*Draft version October 29, 2018*

### ABSTRACT

We present measurements of the optical/UV emission lines for a large homogeneous sample of 993 quasars from the Large Bright Quasar Survey. Our largely automated technique accounts for continuum breaks and galactic reddening, and we perform multicomponent fits to emission line profiles, including the effects of blended iron emission, and of absorption lines both galactic and intrinsic. Here we describe the fitting algorithm and present the results of line fits to the LBQS sample, including upper limits to line equivalent widths when warranted. The distribution of measured line parameters, principally  $W_\lambda$  and FWHM, are detailed for a variety of lines, including upper limits. We thus initiate a large-scale investigation of correlations between the high energy continuum and emission lines in quasars, to be extended to complementary samples using similar techniques. High quality, reproducible measurements of emission lines for uniformly selected samples will advance our understanding of active galaxies, especially in a new era of large surveys selected by a variety of complementary methods.

*Subject headings:* galaxies: active — quasars: emission lines — quasars: general — ultraviolet: galaxies

### 1. INTRODUCTION

Quasars, some of the most luminous objects in the Universe, allow us to observe towards the start of cosmic time, probing extremes of physics, and illuminating the intervening matter. Though most of the QSOs now known were discovered by their unique spectral energy distributions (SEDs) or emission lines, several interrelated and fundamental questions remain:

- 1) What significant correlations exist between the observed SED and emission lines in large uniform quasar samples?
- 2) How are the observed SED and emission lines affected by intrinsic absorption and orientation?
- 3) Can the shape of the intrinsic SED be determined?
- 4) What effect does the intrinsic SED have on emission lines and what does that tell us about physical conditions in the QSO?

The production of emission lines in QSO spectra is widely attributed to photoionization and heating of the emitting gas by the UV to X-ray continuum (e.g., Ferland & Shields 1985; Krolik & Kallman 1988). Emission lines from a given ion are particularly sensitive to photons of energy above the corresponding ionization threshold, but ionization from excited states and heating via free-free and H<sup>-</sup> absorption also determine the line's principal ion-

izing/heating continuum. Many important lines respond to the extreme ultraviolet (EUV) or soft X-ray continuum. Unfortunately, the EUV band is severely obscured by Galactic absorption, although some constraints on the EUV ionizing continuum are available through analysis of the adjacent UV and soft X-ray windows.

The overall similarity of QSO emission line spectra has on occasion been taken as evidence of fairly uniform physical conditions in the broad emission line region (BELR). At first, this encouraged the assumption that clouds in the BELR inhabit a narrow swath of parameter space in density, size, and ionization parameter ( $U$ ). Observed correlations of line equivalent widths (hereafter,  $W_\lambda$ ) with SEDs present challenges to geometric and photoionization models that need to be answered. Photoionization pioneers such as Mushotzky & Ferland (1984) ran models on a single cloud, while photoionization models assuming a distribution of clouds (i.e., not a single  $U$ ) predict a strong dependence of  $W_\lambda$  on the (assumed power law) slope of the SED (Binette et al. 1989; Baldwin et al. 1995; Korista, Baldwin, & Ferland 1998).

Large uniform samples of QSO emission line measurements are key to test photoionization models, but are also necessary for other important tests of quasar triggering and evolution. Tests of the binary vs. lens hypothesis

for quasar pairs at the same redshift require quantitative measures of the probability of finding the measured spectral similarity derived from complete samples (Mortlock, Webster & Francis 1999). Since optically-selected QSOs at similar redshift may tend to be more similar than 2 QSOs chosen entirely at random, studies of QSO spectral properties should be based on samples large enough to provide statistically significant subsamples across a wide range of luminosity and redshift (Peng et al. 1999).

In a small, complete sample of optically-selected QSOs studied by Laor et al. (1997), the strongest correlation found between X-ray continuum and optical emission line parameters was of the soft X-ray spectral slope ( $\alpha_x$ ), and the FWHM of H $\beta$ . Strong correlations between  $\alpha_x$  and the relative strengths of [O III]  $\lambda$ 5007 and iron emission were seen both there and in previous studies, particularly Boroson & Green (1992) (hereafter BG92). A principal component analysis (PCA) was employed by BG92 to examine an unwieldy set of emission line and continuum correlations within a sample of 87 QSOs taken from the Palomar-Green Bright Quasar Survey (BQS; Schmidt & Green 1983). This indicated that the strongest sources of variance in the optical spectra, the “primary eigenvector”, involved an anti-correlation between the strength of [O III]  $\lambda$ 5007 and iron emission that was also linked to the FWHM of H $\beta$ . This work was extended by Marziani et al. (1996) (hereafter M96) and Sulentic et al. (2000) to include a study of the spectral region around C IV  $\lambda$ 1549. These papers identified Narrow-line type 1 Seyfert galaxies (NLS1) and steep spectrum radio galaxies as occupying opposite ends of the primary eigenvector. Other work utilizing the high spectral resolution of the *Hubble Space Telescope* Faint Object Spectrograph (*HST* FOS) showed a link between Al III  $\lambda$ 1859, Si III]  $\lambda$ 1892, and C III]  $\lambda$ 1909 emission line strengths and the primary eigenvector but suffered from the small sample size and a focus on NLS1 or the low redshift radio quiet objects in the BQS (Aoki & Yoshida 1999; Kuraszkiewicz et al. 2000).

The samples of AGN used by most authors are almost entirely taken from BG92 and so do not represent a statistically complete sample and may not be truly representative of the QSO population (Wisotzki et al. 2000). They also deal with the strongest emission features in the OUV spectrum and, while several hypotheses have been proposed, the physical origin of the observed correlations remains a puzzle. There is also a concern that biases within these small samples may have exaggerated the significance of the primary eigenvector.

Even in the clear presence of extrinsic effects such as absorption along the line of sight, emission lines have been used to infer the strength and shape of the high energy SED. As an example, the similarity of UV emission-line properties in broad absorption line (BAL) and non-BAL QSOs (Weymann et al. 1991) has been cited as evidence that orientation is the cause of the BAL phenomenon (i.e., that *all* radio-quiet QSOs have BAL clouds). However, BALQSOs are now known to exhibit markedly weak X-ray emission as a class (Green & Mathur 1996; Gallagher et al. 1999; Brandt, Laor, & Wills 2000). But if similar emission lines indeed vouch for similar intrinsic high energy SEDs, then the large X-ray to optical continuum flux ratio ( $\alpha_{ox}$ ) values observed for BALQSOs are likely to be

caused by strong absorption along the line-of-sight rather than by differences in their intrinsic SEDs. In fact, the soft X-ray deficit requires absorption at least an order of magnitude larger than those estimated from optical/UV (OUV) spectra alone and the UV and X-ray absorbers have yet to be definitively identified as one (e.g., see discussion in Mathur, Wilkes, & Elvis 1998). Since BALQSOs may be heavily absorbed, the question of whether similar emission lines are testimony for similar intrinsic SEDs must be answered through the systematic study of line and continuum correlations in *unabsorbed* QSOs.

Even in supposedly unabsorbed QSOs, a strong inverse correlation exists between optical iron emission, and O III  $\lambda$  5007 in QSOs (BG92). Iron emission is under-predicted by a large factor in standard photoionization models relative to observations (Collin & Joly 2000), and the continuum source responsible for creating rest-frame optical iron emission lines comes almost entirely from X-rays above about 1keV. QSOs with large  $\alpha_{ox}$  of which BALQSOs represent an extreme, have not only weak O III, but feeble narrow line emission in general (Green 1996). We suggest that the observed correlations may be an effect of absorption of the intrinsic high energy continuum by thick clouds interior to the NELR. The X-ray heating of these clouds makes them emit copious Fe II, lines, but prevents the ionizing continuum from reaching the NELR. This is reinforced by another observed correlation - that the most highly absorbed BALQSOs, the low-ionization BALQSOs, albeit X-ray quiet, are generally very strong optical Fe II, emitters (Stocke et al. 1992; Lipari, Terlevich, & Macchetto 1993). Our interpretation needs to be tested across a range of absorption, in large representative QSO samples.

We have therefore undertaken a major study of quasar line emission, with careful accounting for absorption lines and blended iron emission, using largely automated procedures on carefully-selected samples. The analysis of samples of QSOs with more than a few hundred spectra requires some amount of automation to give consistent results. The largest sample of QSO spectra currently available is that of the Large Bright Quasar Survey and here we describe the initial results from the measurement of this sample and the analysis methods that will also be applied to other large samples of QSO spectra that will become available in the near future.

## 2. THE LBQS SAMPLE

The Large Bright Quasar Survey (LBQS; see Hewett, Foltz & Chaffee 1995) is a sample of 1058 QSOs selected using the Automatic Plate Measuring Machine from UK Schmidt photographic direct and objective prism plates. The combination of quantifiable selection techniques, including overall spectral shape, strong emission lines, and redshifted absorption features has been shown to be highly efficient at finding QSOs with  $0.2 < z < 3.3$ , a significantly broader range than previous work. The LBQS thus avoids selection effects common in other optical quasar samples that tend to exclude weak-lined quasars or to under-sample certain redshift ranges or colors. There appears to be a deficiency in the numbers of QSOs with  $z \sim 0.8$  in the LBQS sample, although the effect is not statistically significant (Hewett et al. 1995). The LBQS has

been for the last decade the principal source of intermediate brightness optically-selected quasars available; 1/9 of the Veron-Cetty & Veron (1998) catalog of QSOs and  $\sim 50\%$  of all known quasars within a similar magnitude range. Radio data are currently available for about 1/3 of the sample (Hooper et al. 1995) and soft X-ray fluxes and upper limits for at least 85% of the sample can be obtained from the *ROSAT* All-Sky Survey. Follow-up optical spectra with  $S/N \approx 10$  in the continuum at  $4500\text{\AA}$  and  $6 - 10\text{\AA}$  resolution were obtained between 1986 and 1990 at the MMT on Mt Hopkins, Arizona and the 2.5m duPont in Las Campanas, Chile for all LBQS QSOs. Error spectra ( $1\sigma$ ) are available for 1009 of the objects. The selection criteria and observing procedures for each of the survey fields can be found in Hewett et al. (1995) and references therein (LBQS Papers I-VI). Three QSOs appear here that were identified subsequently to the 1055 QSOs in the Hewett et al. (1995) LBQS catalog. They are 0052+0148 ( $z=0.595$ ), 1027-0149 ( $z=0.754$ ), and 2132-4227 ( $z=0.569$ ), see Hewett, Foltz, & Chaffee (2001; in preparation) for further details.

### 3. ANALYSIS OF THE SPECTRA

The LBQS spectra were analyzed using *Sherpa*<sup>1</sup>, a generalized fitting engine designed primarily for spatially resolved spectroscopy of observations with NASA's *Chandra* X-ray Observatory. *Sherpa* enables data to be modeled using a variety of optimization methods and with a number of built-in statistical tests. The ease with which user-models can be created and the ability to simultaneously model a number of input data sets that may be in different formats (e.g. modeling an ASCII and a PHA style FITS file together) makes *Sherpa* suitable for our goals. In brief, the process begins with modeling the continuum emission and then accounting for any emission by iron complexes in the spectra. We then model the emission lines using Gaussian profiles and, after a search for significant absorption features, the results are inspected and the emission line fitting procedure repeated to improve the model of each spectrum. The model parameters were determined from a minimization of the  $\chi^2$  statistic with modified calculations of uncertainties in each bin (Gehrels 1986). We found that a Powell optimization method gave a balance between an efficient processing time and consistency of results. Because of the large database of observations the modeling of the spectra proceeds in a largely non-interactive manner.

We do not present measurements of emission lines for objects with strong BALs. The diversity in the strength and shape of BALs precludes even semi-automated measurements, and their emission line properties have already been well-characterized for a strongly overlapping sample in Weymann et al. (1991). We also exclude objects that have multiple narrow absorption features that significantly mask the true shape and strength of the emission features of Lyman  $\alpha$  and C IV  $\lambda 1549$ . A list of the 65 objects excluded from this study can be found in Table 1. This list includes two objects not previously classified as BAL in LBQS papers I-VI, 0059-2545 and 1242+1737. The measurements for the remaining 993 LBQS spectra are presented here.

### 3.1. The continuum

Our first step is to model the continuum emission by fitting one or two power laws to ranges in the spectrum that are free from any strong emission lines. We found the second power law component to be necessary due to the steepening of the continuum towards the UV in low redshift objects, i.e. for spectra that extended redward of rest frame  $4200\text{\AA}$ . A list of the continuum modeling 'windows', along with the nearest strong emission lines, can be found in Table 2. We apply a Galactic reddening correction to the power law continua that follows the prescription given by Cardelli, Clayton, & Mathis (1989) which uses:

$$A(\lambda) = E(B - V)[aR_V + b]$$

where  $a$  and  $b$  are polynomial functions of wavelength derived for  $3.3\mu\text{m} \geq \lambda \geq 1000\text{\AA}$ . We use a ratio of total to selective extinction of  $R_V = 3.1$ , the standard value for the diffuse ISM, and take the relationship between the color excess and the line of sight column of neutral Hydrogen for each object to be

$$E(B - V) = \frac{N_{\text{H}}(\text{Galactic})(10^{20}\text{cm}^{-2})}{58.0}$$

(Bohlin, Savage, & Drake 1978).

Many of the spectra in the LBQS sample depart from a simple reddened power law continuum for wavelengths blueward of  $\sim 4000\text{\AA}$  in the observed frame as noted in the original LBQS papers. This depression in the observed ultraviolet is due to the use of 2.5 arcsecond circular apertures in the MMT observations coupled with the effects of atmospheric dispersion at large zenith distances and a guider system that was red-sensitive. To model this part of the continuum, we use a polynomial of up to 2nd order with the flux tied to that of the power law continuum model in the nearest continuum window with  $\lambda_c$  (observed frame)  $> 4000\text{\AA}$ . We did not apply a polynomial continuum to objects with  $z \geq 2.42$  because the Lyman  $\alpha$  emission line appears redward of  $4000\text{\AA}$  and the continuum on the blue side of Lyman  $\alpha$  can be significantly reduced by Lyman  $\alpha$  forest lines.

The polynomial continuum model is not physically meaningful and may be inaccurate, particularly where strong iron emission complexes appear around the Mg II  $\lambda 2800$  emission line, i.e. for

$$2200\text{\AA} \lesssim \lambda_{\text{rest}} \lesssim 3100\text{\AA}$$

We investigated the effect of the polynomial continuum on  $W_{\lambda}$  measurements and on the error estimates for the emission line parameters by comparing lines of the same species that occurred in the polynomial continuum region to those that did not. A Kolmogorov-Smirnov test (e.g., Press et al. 1992) shows that the distributions of  $W_{\lambda}$  measurements for the UV iron emission, Si IV+O IV  $\lambda 1400$ , C IV, and Mg II emission lines are significantly different when measured above the polynomial continuum compared to when measured using a power law continuum. The median increase in  $W_{\lambda}$  for C IV and Mg II

<sup>1</sup>*Sherpa* is available from the *Chandra* science center (<http://asc.harvard.edu>).

is  $\sim 20\%$  when these lines fall above the polynomial continuum but genuine observational trends like the Baldwin Effect (Baldwin 1977; Osmer, Porter, & Green 1994) may account for this measurement trend. The intrinsic continuum luminosity of objects with C IV redshifted to  $\lambda$  (observed frame)  $> 4000\text{\AA}$  is on average twice that of the lower redshift objects where C IV falls above the polynomial continuum. A 20% increase in  $W_\lambda$  for C IV and Mg II is predicted using the relationships between  $W_\lambda$  and continuum luminosity determined by Zamorani et al. (1992) but may not fully account for the differences seen in the measurements of  $W_\lambda$  for these and other emission lines. Rather than correcting for this effect, we added a systematic uncertainty of 20% to the estimation of emission line strengths and upper limits for all emission lines measured above the polynomial continuum.

Finally, we visually inspected the continuum model for each observation, and found that minor adjustments were required in  $\sim 20\%$  of the sample; a large proportion of these were caused by strong intrinsic absorption lines.

### 3.2. Iron emission

Our second step accounts for iron emission line complexes in the spectra. This emission occurs most strongly in the regions around the Mg II  $\lambda 2800$  and  $H\beta$  emission lines. We follow the prescription used by BG92 of subtracting a template of iron emission lines created from the spectrum of I Zw 1, an NLS1 which exhibits the typically strong iron emission of this class of AGN. We use two templates: the optical emission line template is identical to that used by BG92 and corrects for iron emission between  $4400\text{\AA} < \lambda_{\text{rest}} < 7000\text{\AA}$ , while the UV template was developed by Vestergaard & Wilkes (2000) from *HST* FOS observations of I Zw 1 and covers the region  $1250\text{\AA} < \lambda_{\text{rest}} < 3100\text{\AA}$ . The FWHM of the iron emission features seen in I Zw 1 is similar to that of the  $H\beta$  emission line ( $900 \text{ km s}^{-1}$ ) and so sets the minimum template FWHM. We convolved this template with a series of Gaussian functions of increasing width to produce a grid of 38 template spectra with  $900 \lesssim \text{FWHM} \lesssim 10000 \text{ km s}^{-1}$ , conserving the total flux in each template. This provides us with a nominal resolution of  $250 \text{ km s}^{-1}$ , more than adequate for the quality of the spectra in the LBQS sample.

The first part in modeling the iron emission is to compare the  $2000 \text{ km s}^{-1}$  templates to windows in each spectrum on both sides of the Mg II  $\lambda 2800$  emission line and redward of C III]  $\lambda 1909$  for the UV emission, and to either side of the  $H\beta + [\text{O III}] \lambda\lambda 4959, 5007$  complex for the optical emission (see Table 2). After the relative amplitude of the iron emission has been modeled, the full grid of templates is applied to the spectra to determine the approximate FWHM of the iron emission. This is followed by a final modeling of the template amplitude simultaneously with the FWHM of the template spectra. Adjustments are made from a visual inspection of the results to give the best representation of the iron emission complexes present in each spectrum.

Note that we measure the strengths of the iron emission in the UV and optical independently. This is important as the relative strength of the UV and optical iron emission may allow an approximate determination of the conditions in the emitting region, e.g. density and  $U$  (Verner

et al. 1999). UV and optical iron emission may also correlate differently with X-ray emission. Green et al. (1995) found that QSOs in the LBQS with strong UV Fe II emission (based on the iron feature under  $[\text{Ne IV}]\lambda 2423$ ) are anomalously X-ray bright in the *ROSAT* passband. By contrast, several studies (e.g., Corbin 1993, Lawrence et al. 1997) find an anti-correlation between soft X-ray luminosity and  $R(\text{Fe II})$  (the equivalent width ratio of optical iron emission to  $H\beta$ ). Several such intriguing correlations have been noted, but among samples of varying size and using heterogeneous measurement techniques. Our project attempts to remedy this situation using large samples and uniform analysis.

When first scaling the UV iron template in the LBQS spectra to the iron emission complexes straddling Mg II ( $\sim \lambda\lambda 2200 - 3300$ ), we found that the template tended to over-predict the iron emission line strength blueward of C IV  $\lambda 1549$ . This occurred in 27 of the 238 spectra that cover both C IV and Mg II and that have measurable iron emission. The UV iron template is based on an *HST* FOS spectrum of I Zw 1 for which the region blueward of C IV was observed six months earlier than the remaining spectrum. I Zw 1 clearly brightened between the two observations, for which reason the bluest sub-spectrum was scaled to match the redder spectrum. The reasons for the over-prediction of iron flux blueward of C IV in our sample when using the I Zw 1 template are not clear, but may include a change in iron emission strength and multiplet ratios with luminosity indicating variations in the physical conditions to which the iron emission is sensitive (e.g. Netzer 1980). See Vestergaard & Wilkes (2000) for further details and discussion. To compensate for this effect, the UV iron template flux in the region  $\lambda_{\text{rest}} < 1530\text{\AA}$  was reduced by 50%, resulting in an improved agreement with all the sample spectra.

### 3.3. Emission lines

The emission lines in the spectra are modeled by the addition of Gaussian features at the expected wavelengths to the continuum + iron template model. The initial value of the peak flux near the position of the line is estimated from the raw data assuming a continuum level under each emission line calculated by fitting a straight line between the continuum windows nearest the line to be modeled. The initial estimate of the FWHM of the emission line component is assumed to be  $3000$  to  $5000 \text{ km s}^{-1}$  for broad components, and  $350 \text{ km s}^{-1}$  for narrow components. These reflect the typical widths of emission lines produced in the BELR and NELR (e.g. Peterson 1997). Where the S/N in the spectra are high enough, the Lyman  $\alpha$ , C IV, Mg II, and  $H\beta$  emission lines may be modeled using two Gaussian components. The initial value of the peak amplitude of each component is set to be 40% of the peak flux estimated from the data. Lower S/N spectra are modeled with a single Gaussian but a visual inspection of the results is made and a second Gaussian component is added where significant residuals appear.

The FWHM and peak amplitude of the Gaussian model components are then optimized within a spectral region covering the emission line. The position of the emission line is fixed at the expected wavelength in the initial modeling until after the presence of narrow absorption features

has been determined (§3.4). The region of the spectrum used in modeling an emission feature is chosen to best optimize the component of interest, e.g. the Lyman  $\alpha$  emission line is simultaneously fitted with N V  $\lambda 1240$  and O I  $\lambda 1305$  because the broad component to Lyman  $\alpha$  may have a significant effect on the spectrum near O I. A list of the emission lines modeled in the LBQS spectra is presented in Table 3. There are a number of important emission lines (e.g. C II  $\lambda 1336$ ) that are not modeled here due to the quality of the spectra, but will be included in the application of this procedure to samples of higher spectral resolution (e.g. *HST* FOS spectra).

### 3.4. Absorption lines

One of the goals of this study is to determine the frequency of occurrence of absorption in the spectra of QSOs. We used the program FINDSL (Aldcroft 1993) to detect significant narrow absorption features and model them with multi-component Gaussian fitting. Our input to FINDSL is the sum of the reddened continuum, iron template(s) and all the emission line profiles from the first *Sherpa* modeling. This constitutes a ‘continuum’ from which FINDSL detects significant deviations in the observed spectrum. We rescale the error array of each spectrum for use with FINDSL so that  $\chi^2_\nu$  becomes unity, which yields a better estimate of the true error array and aids in the detection of significant absorption features. We exclude the Lyman  $\alpha$  forest region blueward of rest frame 1065Å from the absorption line detection, and also exclude the Balmer continuum region (between 3360Å – 3960Å) where the global continuum model may lie below the spectrum causing many spurious absorption lines to be detected.

The absorption line measurements from FINDSL were then included with the emission line and continuum results for further modeling using *Sherpa*. In this second iteration the emission line positions are also fitted, and the absorption lines modeled simultaneously with the emission line components. The results from this automated process were inspected and adjustments made to those spectra that the algorithms could not successfully model. This was not unexpected as the wide variety of spectra in the sample and the chance superposition of absorption features on the emission lines makes it unlikely that any fully automatic procedure would be 100% successful.

### 3.5. Error analysis

An estimate of the  $2\sigma$  error range for each parameter of the continuum and emission line components was determined from the  $\chi^2$  confidence interval bounds ( $\Delta\chi^2 = 4.0$ ). Where the amplitude of an emission line could not be constrained to within  $2\sigma$ , the line position was reset to the expected wavelength and the FWHM to a median value that was determined from the distribution of well constrained emission line measurements within the LBQS sample. These fixed emission line parameters are given in Table 3. The emission line amplitude was then re-fitted and, if remaining unconstrained at the  $2\sigma$  level, then the  $2\sigma$  upper limit on the amplitude was estimated. The determination of upper limits for lines that may be present at low flux levels in the spectra of QSOs is one of the pri-

mary objectives of this work. This allows the use of survival analysis techniques in determining a more realistic distribution of emission line strengths.

## 4. EMISSION LINE RESULTS

The total number of emission lines measured from the spectra in the LBQS sample are presented in Table 4. The numbers of upper limits measured and the number of two component emission lines are also tabulated. The full table of all emission line measurements and uncertainties of the 993 spectra modeled here is available from the ApJ in the electronic journal at <http://www.journals.uchicago.edu/ApJ/>, but due to the large size cannot be reproduced in the printed journal. To show the form and content of the large electronic table we present in Table 5 a digested version containing measurements of the emission lines present in three LBQS spectra. The emission line measurements are quoted to a significance level determined by the  $2\sigma$  uncertainties in the parameters (e.g. Bevington & Robinson 1992). The format is as follows: Each object is represented by a row containing the designation and redshift followed by a row for each measured emission line. The name of the emission line is given in column (1), column (2) gives the FWHM in  $\text{km s}^{-1}$ , and column (3) gives the offset of the peak of the Gaussian emission line model, in  $\text{km s}^{-1}$ , from the expected position based on the tabulated redshift. Note that no peak offset measurements appear for the iron emission line measurements. Column (4) gives the rest frame equivalent width of the emission line in Å. Each emission line parameter is quoted with positive and negative  $2\sigma$  error estimates. The errors quoted for  $W_\lambda$  are based in the uncertainties in the amplitude and FWHM of the Gaussian model and do not include an error from an uncertainty in the underlying continuum flux level. For emission lines where only an upper limit on  $W_\lambda$  could be measured, there are no values quoted for the peak offset because we fixed the position of the line at its expected wavelength. The FWHM value also has no associated errors in such a case because it was fixed at an approximate median value for the sample. (See §3.5.) Note that some detected but poorly constrained lines may have an error estimate for the  $W_\lambda$  measurement even while the FWHM is fixed (see §3.5 and Table 4). Finally, column (5) gives the number of narrow absorption features used in modeling the emission lines. They are tabulated in the row of the closest emission line to the position of the absorption feature, e.g. see Lyman  $\alpha$  (broad) and O I for LBQS 2354–0134 in Table 5. The format of the electronic version of Table 5 is explained in the Appendix.

To generate a measure of the strength of iron emission in each spectrum, the integrated flux of the model template in the regions 2240Å – 2655Å (blueward of Mg II) or 4434Å – 4684Å (blueward of H $\beta$ ) is used and combined with the continuum specific flux at 2448Å and 4559Å respectively to calculate  $W_\lambda$ . For objects where these regions were not present in the observed spectrum, we extrapolate the continuum to these positions. Note that we integrate the optical iron template flux over a wavelength range that matches the window used by BG92.

We present in Table 6 the continuum parameters for the same LBQS spectra that appear in Table 5. The full table

is available in electronic form with one row for each QSO in the sample. The format of Table 6 is as follows. Columns (1), (2) and (3) give the QSO designation, redshift, and the Galactic neutral Hydrogen Column density (in units of  $10^{20} \text{ cm}^{-2}$ ) respectively. The latter measurements are taken from the Bell Laboratory H I survey (Stark et al. 1992). Columns (4) - (6) contain the measured values of the power law continuum; continuum slope, the *rest frame* wavelength at which the continuum is normalized, and the continuum flux at that wavelength ( $\text{ergs cm}^{-2} \text{ s}^{-1} \text{ \AA}^{-1}$ ) respectively, along with their  $2\sigma$  uncertainties. Note that in Table 6 the normalization units are  $10^{-16}$  but in the electronic table the units are  $10^{-14}$ . Column (7) lists the slope of the second power law continuum if used, the normalization of which is identical to the first power law continuum. Column (8) presents the order of the polynomial continuum if required to model the blue region of the spectra. The format of the electronic version of Table 6 is explained in the Appendix.

We present in Figures 3a, 3b, and 3c the profiles and residuals from the models of the three spectra presented in Tables 5 and 6. The measurements presented here were chosen to show a range of spectral qualities present in the LBQS sample. Fig. 3 includes a number of panels for each spectrum in each case all wavelengths are observed frame and fluxes are  $10^{-14} \text{ ergs cm}^{-2} \text{ s}^{-1} \text{ \AA}^{-1}$ . The top panel has three sections, the upper section shows the continuum model overlying the spectrum, including error bars on each bin, the middle section displays the iron emission template plotted over the spectrum (no error bars) and the lower section shows template profile alone. Note that the flux scales are different in these sections to display the template emission more clearly.

This panel is followed by a number of separate panels, one for each emission line region. These emission line panels have three sections; the top section shows the total continuum + emission line model over the spectrum. (The model will include flux from the iron emission line template(s) if used. For clarity, flux errors on each bin are not shown in this section.) The middle section shows the residuals from the emission line model and include the error bars for each spectral bin. The lower section shows the profiles of the emission line models, with multiple components separated into single Gaussian profiles. The shape of the iron emission template used in the modeling of the spectrum is also shown in the lower panel. Dashed vertical lines indicate the expected position of emission lines based on tabulated redshifts. Absorption line profiles are shown along the top edge of the lower panels, e.g. the Lyman  $\alpha$  region panel for LBQS 2354–0134 in Fig.3c. For the panels that show the emission line models of [Ne V], [O II], and [Ne III] the top sections also plot the local continua used for these lines (see Appendix). Note that to help visualize the quality of the emission line models the wavelength scale is identical for each of the emission line panels and within each panel the flux scale is identical in the sections displaying the total model, residuals, and individual model components.

## 5. OVERALL STATISTICS

The analysis of the LBQS sample of QSO spectra has provided us with over 8000 emission line measurements, of

which approximately 30% are upper limits to the equivalent width of low intensity lines. Without the correct inclusion of these “censored” data in the analysis of this complete sample, a biased estimation of the properties may occur and a number of important relationships may be masked or, even worse, appear more significant than in reality.

We use a non-parametric survival analysis technique to estimate the means and medians that characterize the emission line parameter distributions. The Kaplan-Meier (KM) estimator of a sample distribution is a maximum likelihood method that provides a reconstruction of information lost by censoring of data. This well established statistical technique has been thoroughly examined for use in astronomical studies by Feigelson & Nelson (1985), Isobe, Feigelson, & Nelson (1986) and references therein. We recommend these papers to the reader.

The astronomical survival statistics package ASURV Rev 1.1 (Isobe & Feigelson 1990; LaValley, Isobe & Feigelson 1992) was used to provide the means, errors on the mean, and the medians of the  $W_\lambda$  distributions for the LBQS sample given in Table 7 and the distributions of  $W_\lambda$  shown in Figure 4. The format of Table 7 is as follows. Column (1) lists the emission line or line blend measured. The distribution for single Gaussian component models are tabulated separately from narrow and broad components. The distribution of sum of the  $W_\lambda$  of the broad and narrow component models included with the single component measurements is also tabulated. Columns (2) to (4) give the number of detected emission lines, their mean  $W_\lambda$  and the standard deviation (SD) of the distribution of  $W_\lambda$ . Columns (5) and (6) list the total number of emission lines measured for each species and the number of upper limits estimated for  $W_\lambda$ . Columns (7) and (8) give the KM means, error on the means, and medians of  $W_\lambda$  for each line. Columns (9) to (11) give the number, mean and median of the FWHM of the Gaussian components used to model each emission feature. All equivalent widths are rest frame and the error on the  $W_\lambda$  means is estimated from the  $1\sigma$  of the KM reconstructed distribution. Note that there are no upper limit measurements for two component emission line fits, in cases where any of the parameters of the two components could not be constrained to  $2\sigma$ , a single Gaussian was used to model the line.

We should add a note of caution here about the reconstructed distribution of emission line properties for samples that contain a large proportion of censored data (e.g. [Ne V], He II  $\lambda 4686$ ). Formally, an emission line is detected if the amplitude of a feature can be constrained to within  $2\sigma$ , based on the  $\chi^2$  confidence interval bounds. The performance of the KM estimator degrades if the censored fraction is high or if the pattern of censored measurements is not random. We do not believe the latter is a concern here because the observing procedure used in the generation of the sample spectra produced spectra of similar continuum S/N, independent of the strength of emission features and the intrinsic luminosity of the QSO. In support of this conclusion consider the statistics of the O I emission line, where approximately half of the spectra with coverage in the region of this line possess detected emission features. Detected emission lines have  $0.6 \lesssim W_\lambda \lesssim 14.0$

$\text{\AA}$  but the range of upper limits for the undetected lines is  $0.2 \lesssim W_\lambda \lesssim 15.0 \text{\AA}$ . The large proportion of censored data for some emission lines lowers our confidence in the KM estimate of the means and medians of a reconstructed  $W_\lambda$  distribution. Any conclusions based on these emission lines should rather use the results from the detected lines alone.

The histograms shown in Figure 4 are taken from the KM estimation of the number of data points in each bin. The  $W_\lambda$  ( $\text{\AA}$ ) and FWHM ( $\text{km s}^{-1}$ ) distribution for each emission line are shown in the upper and lower panels for each emission line respectively. For emission lines that have been modeled using two Gaussian components, we include the distribution for the narrow and the broad components separately from the single component lines. For completeness we also show in Figure 4 the distribution of the full sample of measured lines where the  $W_\lambda$  of broad+narrow components of an emission line have been summed and included in the single component distribution (dashed line histograms).

## 6. DISCUSSION

To examine the robustness of the analysis procedure in OUV spectra with improved S/N and spectral resolution we have modeled two composite QSO spectra using the techniques described above. The first was constructed by Francis et al. 1991 (hereafter F91) from 718 spectra in the LBQS sample itself, and the second from *HST* FOS observations of 101 QSOs presented in Zheng et al. (1997) (hereafter Z97). We find that even where the limit of two Gaussian components for an emission line does not reproduce the line profile very well, the measured  $W_\lambda$  is within 10% of values tabulated in the above papers. The exception is for Mg II where the F91 measurement is higher and the Z97 measurement is lower than that measured using the techniques presented above. Both discrepancies can be attributed to the presence of iron emission features blending into the wings of the Mg II emission line. Although F91 fitted a global continuum and corrected for iron emission using local spline fits to emission complexes, the  $W_\lambda$  was measured as the total flux above the continuum and iron emission across more than  $50 \text{\AA}$  in the spectrum and so may include some hidden iron emission. This is also likely to be the explanation of a similar discrepancy in the measurements of  $\text{H}\gamma + [\text{O III}] \lambda 4363$  and  $[\text{O III}] \lambda 4959$  in the F91 composite. The measurements in Z97 use a local continuum which is difficult to determine accurately in regions where iron emission complexes are strong, and may result in their lower  $W_\lambda$  measurement. This confirms that correct accounting for iron emission is crucial in the measurement of emission lines in QSO spectra.

We can also compare the global properties of the LBQS emission line measurements with the measurements of these composite QSO spectra. The Z97 composite shows larger  $W_\lambda$  in Lyman  $\beta + \text{O VI}$ , Lyman  $\alpha$ , and C IV. The discrepancy remains even if the means of only our detected emission lines are compared. (The inclusion of the censored data will naturally lower the means of a distribution, but has little effect on the distribution of strong lines like Lyman  $\alpha$  and C IV which are well constrained in nearly all cases). We suspect that the difference is attributable to the large (60%) fraction of radio loud ob-

jects in the heterogeneous sample used to construct the Z97 composite. The LBQS sample is predominantly Radio Quiet (RQ) with  $\sim 10\%$  Radio Loud (RL) (Hooper et al. 1995) and Z97 showed that there are significant differences in the strength of these lines between RL and RQ populations, independent of luminosity. A marginally significant RL/RQ difference was also seen in a sample of 255 of the optically brightest QSOs in the LBQS sample (Francis, Hooper, & Impey 1993). A more detailed examination of this effect will be made in a subsequent paper that will contrast the continuum and emission line properties within the full LBQS sample.

In contrast, the  $W_\lambda$  of the emission features in the F91 composite are lower than the mean and medians of the measured emission lines in the LBQS sample. Although the F91 composite was created using a large proportion of the same spectra measured here, it is not surprising that the measurements should differ. Lyman  $\alpha$ , which shows the largest dispersion of relative flux within the sample (see Fig. 5 in F91), is most affected by narrow absorption features. Allowance for the effects of narrow absorption increases the  $W_\lambda$  modeled with Gaussian components relative to an estimate based on the integration of flux above a continuum. For  $[\text{Ne III}]$  and  $\text{H}\delta$ , the F91 composite indicates a stronger feature than suggested by the KM mean presented in Table 7. However, the measurements are similar when only the detected lines are studied.

There has been no investigation of inclusion of censored data on the emission line and continuum correlations, particularly the Baldwin effect (Baldwin 1977; Zamorani et al. 1992; Osmer, Porter, & Green 1994) and the correlations associated with the primary eigenvector of spectral variance in AGN (BG92, M96, Sulentic et al. 2000). Previous studies have focussed on a small number of bright emission features; particularly C IV  $\lambda 1549$ , He II  $\lambda 4686$ ,  $\text{H}\beta$ , O III  $\lambda 5007$  and iron emission. We briefly summarize the published measurements for QSO samples of BG92 (87 low  $z$  QSOs, optical spectra), McIntosh et al. (1999) (32 high  $z$  QSOs with IR spectra), M96 (52 QSOs with optical and UV spectra) and Sulentic et al. 2000 (125 QSOs) in Table 8. Where upper limits are quoted, we have used survival analysis to enable a more direct comparison to our results in Table 7. Some of the published work has also been presented separately as RL or RQ subsamples. While all these studies suffer from differing selection effects, the comparison samples also differ from the LBQS sample in redshift range and magnitude limits.

The most notable difference between the properties of the LBQS and the measurements shown in Table 8 can be seen in the relative strength of optical iron emission, the mean value of which appears significantly higher in BG92 and M96. The region used to measure the  $W_\lambda$  of optical iron emission is identical to that used in BG92 (and subsequent authors) and a test using the methods described in §3 to measure the BG92 sample spectra (kindly supplied by T. Boroson) shows reasonable ( $\sim 20\%$ ) agreement in  $\text{Fe II } W_\lambda$ . The measurement of UV iron emission in M96 appears similar to the mean of the distribution of iron emission strength measured in the LBQS sample. However the window used by M96 to characterize the iron emission strength was  $1550 - 1750 \text{\AA}$  and the iron template flux in this region is approximately 6.5% of the flux in the region

used for the study of the LBQS sample presented here (i.e. the mean UV iron emission in M96 is 15 times higher than the mean in the LBQS sample!). The unusually strong iron emission was noted by M96 as a possible bias in their sample. The heterogeneous sample (52 AGN for which *HST* FOS spectra covering C IV were available in 1994 and for which the authors had matching optical spectra) has an overabundance of strong iron emitters relative to the BG92 sample. The difference in iron emission distributions contrasts to the similarity seen in the distributions of  $W_\lambda$  for  $[\text{O III}]\lambda 5007$ . The strongest correlations reported for optical spectra of AGN involve iron emission,  $\text{H}\beta$  and  $[\text{O III}]$ . We expect that our new, more homogeneous emission line measurements, of iron in particular, may significantly reshape the discussion of correlations that produce the largest variance in PCA analysis of quasar emission lines.

## 7. SUMMARY

This paper makes available measurements from the largest database of OUV spectra of QSOs to date. Our analysis of 993 spectra of similar quality from the LBQS yields over 8000 measurements of the 20 most prominent emission lines between rest frame 1025Å – 5900Å. We

have accounted for the effects of blended iron emission complexes, narrow absorption lines, continuum breaks, and we include upper limits on the strength of low intensity emission lines. The measurements are presented with uncertainties generated in an objective manner and with a rigorous inclusion of censored data in tabulated emission line parameter distributions. A more exhaustive analysis of the relationships between the emission line and continuum properties of the LBQS sample will be presented in a later paper.

High quality, reproducible measurements of emission lines for uniformly selected samples will advance our understanding of active galaxies, especially in a new era of large surveys selected by a variety of complementary methods, such as the Sloan Digital Sky Survey (SDSS; York et al. 2000), the FIRST Bright Quasar Survey (White et al. 2000), or the Chandra Multiwavelength Project (Green et al. 1999).

The authors gratefully acknowledge support provided by NASA through grant NAG5-6410 (LTSA). CBF acknowledges the support of NSF grant AST 98-03072. KF thanks Matt Malkan and the UCLA Division of Astronomy & Astrophysics for their hospitality.

## REFERENCES

Aldcroft, T.A. 1993, *PhD Thesis*, Stanford University  
 Aoki, K., & Yoshida, M. 1999 in *Quasars and Cosmology* eds. G. Ferland, & J. Baldwin (ASP conference series) v162, p385  
 Baldwin, J.A. 1977, ApJ, 214, 679  
 Baldwin, J.A., Ferland, G., Korista, K., & Verner, D. 1995, ApJ, 455, 119  
 Bevington, P.R., & Robinson, D.K. 1992 *Data reduction and error analysis for the physical sciences* 2nd ed. (McGraw-Hill)  
 Binette, L., Prieto, A., Szuszkiewicz, E., & Zheng, W. 1989, ApJ., 343, 135  
 Bohlin, R.C., Savage, B.D., & Drake, J.F. 1978, ApJ, 244, 132  
 Boroson, T.A., & Green, R.F. 1992, ApJS, 80, 109 (BG92)  
 Brandt, W.N., Laor, A., & Wills, B. J. 2000, ApJ, 528, 637  
 Cardelli, J.A., Clayton, G.C., & Mathis, J.S. 1989, ApJ, 345, 245  
 Chaffee, F.H., Foltz, C.B., Hewett, P.C., Francis, P.A., Weymann, R.J., Morris, S.L., Anderson, S.F., & MacAlpine, G.M. 1991, AJ, 102, 461 (LBQS paper IV)  
 Collin, S., & Joly, M. 2000, New Astronomy Reviews, 44, 531  
 Corbin, M.R. 1993, ApJ, 403, L9  
 Feigelson, E.D., & Nelson, P.J. 1985, ApJ, 293, 192  
 Ferland, G.F., and Shields, G.A. 1985 in *Astrophysics of Active Galaxies and Quasi-Stellar Objects*, ed. J. Miller (Mill Valley, CA: University Science Books), p.57  
 Foltz, C.B., Chaffee Jr., F.H., Hewett, P.C., MacAlpine, G.M., Turnshek, D.A., Weymann, R.J., & Anderson, S.F. 1987, AJ, 94, 1423 (LBQS paper I)  
 Foltz, C.B., Chaffee, F.H., Hewett, P.C., Weymann, R.J., Anderson, Scott F., & MacAlpine, G.M. 1989, AJ, 98, 1959 (LBQS paper II)  
 Francis, P.J., Hewett, P.C., Foltz, C.B., Chaffee, F.H., Weymann, R.J., Morris, S.L. 1991, ApJ, 373, 465 (F91)  
 Francis, P.J., Hooper, E.J., & Impey, C.D. 1993, AJ, 106, 417  
 Gallagher, S. C., Brandt, W. N., Sambruna, R. M., Mathur, S., & Yamasaki, N. 1999, ApJ, 519, 549  
 Gehrels, N. 1986, ApJ, 303, 336  
 Green, P.J., Schartel, N., Anderson, S.F., Hewett, P.C., Foltz, C.B., Fink, H., Brinkmann, W., Trümper, J., & Margon, B. 1995, ApJ, 450, 51  
 Green, P.J., & Mathur, S. 1996, ApJ, 462, 637  
 Green, P.J. 1996, ApJ, 467, 61  
 Green, P.J. et al. 1999, BAAS, 195, 8008  
 Hewett, P.C., Foltz, C.B., Chaffee, F.H., Francis, P.J., Weymann, R.J., Morris, S.L., Anderson, S.F., MacAlpine, G.M. 1991, AJ, 101, 1121 (LBQS paper III)  
 Hewett, P.C., Foltz, C.B., & Chaffee, F.H. 1995, AJ, 109, 1498 (LBQS paper VI)  
 Hooper, E., Impey, C.D., Foltz, C., & Hewett, P. 1995, ApJ, 445, 62  
 Isobe, T., Feigelson, E.D., & Nelson, P.J. 1986, ApJ, 306, 490  
 Isobe, T., & Feigelson, E.D., 1990, BAAS, 22, 917  
 Korista, K., Baldwin, J., & Ferland, G. 1998, ApJ, 507, 24  
 Krolik, J.H., & Kallman, T.R. 1988, ApJ, 324, 714  
 Kuraszkiewicz, J., Wilkes, B.J., Czerny, B., & Mathur, S. 2000, ApJ, in press  
 Laor, A., Fiore, F., Elvis, M., Wilkes, B.J., McDowell, J.C. 1997, ApJ, 477, L93  
 LaValley, M., Isobe, T., & Feigelson, E.D., 1992, in *Astronomical Data Analysis Software and Systems I*, eds. D.M. Worrall, C. Biemesderfer, & J. Barnes (A.S.P. Conference Series, v25, p245)  
 Lawrence, A., Elvis, M., Wilkes, B.J., McHardy, I., & Brandt, N. 1997, MNRAS, 285, 879  
 Lipari, S., Terlevich, R., & Macchetto, F. 1993, 406, 451  
 McIntosh, D.H., Rieke, M.J., Rix, H.-W., Foltz, C.B., & Weymann, R.J. 1999, ApJ, 514, 40  
 Marziani, P., Sulentic, J.W., Dultzin-Hacyan, D., Calvani, M., & Moles, M. 1996, ApJS, 104, 37 (M96)  
 Mathur, S., Wilkes, B., & Elvis, M. 1998, ApJ, 503, L23  
 Morris, S.L., Weymann, R.J., Anderson, S.F., Hewett, P.C., Francis, P.J., Foltz, C.B., Chaffee, F.H., & MacAlpine, G.M. 1991, AJ, 102, 1627, (LBQS paper V)  
 Mortlock, D.J., Webster, R.L., & Francis, P.J. 1999 MNRAS, 309, 836  
 Mushotzky, R.F., and Ferland, G.J. 1984, ApJ, 278, 558.  
 Netzer, H. 1980, ApJ, 236, 406  
 Osmer, P.S., Porter, A.C., & Green, R.F. 1994, ApJ, 436, 678  
 Peng, C.Y., Impey, C.D., Falco, E.E., Kochanek, C.S., Lehar, J., McLeod, B.A., Rix, H.-W., & Keeton, C.R. 1999 ApJ, 524, 572  
 Peterson, B.M. 1997 *An Introduction to active galactic nuclei*, (CUP:UK)  
 Press, W.H., Teukolsky, S.A., Vetterling, W.T., & Flannery, B.P. 1992, *Numerical Recipes in FORTRAN: The Art of Scientific Computing* 2nd ed. (CUP)  
 Schmidt, M., & Green, R.F. 1983, ApJ, 269 325  
 Stark, A.A., Gammie, C.F., Wilson, R.W., Bally, J., Linke, R.A., Heiles, C., & Hurwitz, M. 1992, ApJS, 79, 77  
 Stocke, J.T., Morris, S.L., Weymann, R.J., & Foltz, C.B. 1992, ApJ, 396, 487  
 Sulentic, J.W., Zwitter, T., Marziani, P., & Dultzin-Hacyan, D. 2000, ApJ, 536, L5  
 Verner, E.M., Verner, D.A., Korista, K.T., Ferguson, J.W., Hamann, F., & Ferland, G.J. 1999, ApJS, 120, 101  
 Veron-Cetty, M.-P., & Veron, P. 1998 *A Catalogue of quasars and active nuclei*, 8th ed., (Garching:ESO 1998)  
 Vestergaard, M., & Wilkes, B.J. 2000, ApJ, submitted.  
 Weymann, R.J., Morris, S.L., Foltz, C.B., & Hewett, P.C. 1991, ApJ, 373, 23  
 White R. L. et al. 2000, ApJS, 126, 133

Wisotzki, L., Christlieb, N., Bade, N., Beckmann, V., Köhler, T., Vanelle, C., & Reimers, D. 2000, A&A, 358, 77

York, D. G., et al. 2000, AJ, 120, 1579

Zamorani, G., Marano, B., Mignoli, M., Zitelli, V., & Boyle, B.J. 1992, MNRAS, 256, 238

Zheng, W., Kriss, G.A., Telfer, R.C., Grimes, J.P., & Davidsen, A.F. 1997 ApJ, 475, 469 (Z97)

## APPENDIX

*Notes on specific emission lines*

**Lyman  $\beta$  + O VI  $\lambda 1035$**  — A flat ‘pseudo’ continuum and a single Gaussian emission feature were used to model the spectrum near this emission line blend. The resulting equivalent widths should be viewed as approximate due to the nature of the QSO spectra in this region. Only in one spectrum of the sample was the Lyman  $\beta$  and O VI emission lines clearly distinct, but the spectrum was modeled with a single Gaussian for consistency.

**He II  $\lambda 1640$**  — The single Gaussian component used to model the region on the red side of C IV  $\lambda 1549$  will account for emission from He II  $\lambda 1640$ , [Ne V]  $\lambda\lambda 1575, 1593$ , [Ne IV]  $\lambda\lambda 1602, 1609$ , Si II  $\lambda 1650$ , [O III]  $\lambda\lambda 1661, 1663, 1668$ , & Al II  $\lambda 1670$ . The use of multiple Gaussian components in all but a few spectra did not improve the model fit to this region due to the quality of the LBQS sample. The tabulated values for this emission line component, particularly the FWHM, will be much larger than expected for just the He II line.

**[Ne V]  $\lambda 3426$ , [O II]  $\lambda 3728$ , [Ne III]  $\lambda 3869$**  — The global continuum model was not successful for the region near these lines due to the blend of Balmer emission lines from transitions with  $m \geq 7$  in the low resolution spectra and so a local power law continuum was created. This was measured from windows 30Å wide at least 30Å from the expected line position. The emission lines are measured above this local continuum.

**He II  $\lambda 4686$**  — For spectra where two Gaussian were used to model the H $\beta$  emission line, the H $\beta$  broad component was included in the model fit of the He II  $\lambda 4686$  emission line.

*Individual Objects*

**LBQS 1206+1052** — This QSO was assigned a redshift of  $0.402 \pm 0.005$  (Hewett et al. 1995) based on the cross correlation with the Francis et al. (1991) LBQS composite spectrum. Although all the features in the spectrum will contribute to the redshift estimate the stronger features will contribute more than the weak so it is unclear as to the cause of the discrepancy as the strongest lines of [O III]  $\lambda\lambda 4959, 5007$  are clearly not at the tabulated redshift. Only the measurement of the Mg II emission line agrees with this redshift, this is likely due to the presence of an absorption feature on the blue side of Mg II that is not modeled in the automated fitting procedure used here. Other lines in the spectrum all show a lower redshift. The value adopted here is  $z = 0.396 \pm 0.003$  based on the median of 10 emission measurements and the  $1\sigma$  value of the distribution of  $z$ .

**LBQS 0023+0228** — The spectrum of this QSO shows very strong and narrow (FWHM  $\simeq$  instrumental resolution) forbidden emission lines, no evidence of broad H $\beta$  emission and only a weak flat continuum. The strength of [O II] ( $W_\lambda = 148^{+8}_{-11}$  Å) and [O III] ( $W_\lambda = 258^{+12}_{-14}$  Å) in the spectrum of LBQS 0023+0228 is much higher than all the other QSOs in the LBQS except for LBQS 0004+0224 which shows a rising blue continuum and strong broad emission from Mg II and H $\beta$  as well as having forbidden line FWHM  $\gtrsim 1200$  km s $^{-1}$ . The spectrum of LBQS 0023+0228 resembles that of a starburst galaxy (e.g. M82) rather than a QSO. The presence of these two strong narrow line objects in the sample does not affect the parameter distributions due to the large numbers of objects in each sample.

*Electronic Tables*

The electronic version of Table 5 has an identical format to that published here but includes one row for each emission line that is listed in Table 3 even if the line lies outside the wavelength range of the observed spectrum. The electronic table contains zeros for unmeasured emission line parameters, rather than the (...) present in printed Table 5. This will aid in the use of this large machine readable ASCII table. The first line of the electronic table contains shortened column headings. This is followed by 31 lines for each QSO (a total of 30753 lines). The first line for each object tabulates the QSO designation and redshift and has a format (a10,f6.3). This is followed by 30 rows with a format (a16,6i7,3f9.2,i3), note that the positive and negative error estimates appear in *separate* columns. Where only an upper limit for  $W_\lambda$  of an expected emission line is measured, the value is given in the positive error column of  $W_\lambda$ . The FWHM for these lines is given with zeros in the error columns (the position offset is by definition 0 km s $^{-1}$ ). Note that there are emission lines where the FWHM and position offset could not be constrained but the  $W_\lambda$  is constrained to  $2\sigma$ .

The format of the electronic version of Table 6 is identical to that presented here and as with the electronic version of Table 5, the positive and negative errors have separate columns. The first line of the electronic table contains the column headings and is followed by a single row for each object with the ASCII format (a10,2f6.3,3f7.2,i6,3f11.5,3f7.2,i3). The normalization units for the power law continuum (columns 8, 9, and 10 in the electronic table) are  $10^{-14}$  erg cm $^{-2}$  s $^{-1}$  Å $^{-1}$ . We stress that in the electronic form of Tables 5 and 6 zeros appear in all blank spaces that would normally appear blank.

TABLE 1  
LBQS QSOs EXCLUDED FROM EMISSION LINE MEASUREMENTS

Designation	Redshift	Ref <sup>a</sup>	Notes	Designation	Redshift	Ref <sup>a</sup>	Notes
0004+0147	1.710	II		1230+1627B	2.735	i	1,2
0010-0012	2.154	II		1230+1705	1.420	III	
0013-0029	2.083		1,2	1231+1320	2.380	I	
0018-0220	2.596		1	1235+1453	2.699	I	
0018+0047	1.835	II		1235+0857	2.898	I	
0019+0107	2.130	II		1235+1807B	0.449	I	
0021-0213	2.293	II		1239+0955	2.013	I	
0022+0150	2.826	II		1240+1516	2.297	i	1,2
0025-0151	2.076	II		1240+1551	0.573	iii	5
0029+0017	2.253	II		1240+1607	2.360	III	
0045-2606	1.242	V		1242+1737	1.863		1,2,3,4
0051-0019	1.713	IV		1243+0121	2.796	III	
0054+0200	1.872	IV		1314+0116	2.686	III	
0059-2545	1.955		3,4	1331-0108	1.881	III	
0059-0206	1.321	IV		1332-0045	0.672		6
0059-2735	1.593	V		1333+0133	1.577	iii	2
0100-2809	1.768	V		1442-0011	2.226	III	
0103-2753	0.848	V		1443+0141	2.451	III	
0109-0128	1.758	IV		2111-4335	1.708	V	
1009+0222	1.349	III		2113-4345	2.053	v	1,2
1016-0248	0.717	III		2116-4439	1.480	V	
1029-0125	2.029	III		2140-4552	1.688	V	
1133+0214	1.468	III		2201-1834	1.814	V	
1138-0126	1.266	III		2208-1720	1.210	V	
1203+1530	1.628	III		2211-1915	1.952	V	
1205+1436	1.643	I		2212-1759	2.217	V	
1208+1535	1.961	I		2241+0016	1.394	II	
1212+1445	1.627	I		2244-0105	2.030	ii	1,2,7
1214+1753	0.679	I		2350-0045A	1.617	II	
1216+1103	1.620	I		2351+0120	2.068		1,2
1219+1244	1.309	III		2355-0209	1.802	II	
1224+1349	1.838	I		2358+0216	1.872	IV	
1228+1216	1.408	I					

<sup>a</sup>Original LBQS paper that identified BAL (upper case) or associated narrow absorption (lower case).

NOTE.—1) NAL on Lyman  $\alpha$ ; 2) NAL on C IV; 3) BAL near Lyman  $\alpha$ ; 4) BAL near C IV; 5) NAL on Mg II; 6) BAL near Mg II; 7) NAL on N V.

REFERENCES.—(I,i) Foltz et al. 1987; (II,ii) Foltz et al. 1989; (III,iii) Hewett et al. 1991; (IV,iv) Chaffee et al. 1991; (V,v) Morris et al. 1991

TABLE 2  
CONTINUUM AND IRON FITTING WINDOWS

Rest frame wavelength range (Å)		Emission lines nearby	
Continuum	Iron	Blueward	Redward
1140 – 1150 <sup>a</sup>		O VI $\lambda$ 1035	Lyman $\alpha$ $\lambda$ 1215
1275 – 1280		N V $\lambda$ 1243	O I $\lambda$ 1305
1320 – 1330		O I $\lambda$ 1305	Si IV + O IV $\lambda$ 1400
1455 – 1470		Si IV + O IV $\lambda$ 1400	C IV $\lambda$ 1549
1690 – 1700		He II $\lambda$ 1640	Al III $\lambda$ 1859
2160 – 2180	2020 – 2120	C III] $\lambda$ 1909	Mg II $\lambda$ 2800
2225 – 2250	2250 – 2650		
3010 – 3040 <sup>b</sup>	2900 – 3000	Mg II $\lambda$ 2800	[Ne V] $\lambda$ 3426
3240 – 3270		[O II] $\lambda$ 3728	[Ne III] $\lambda$ 3869
3790 – 3810		H $\delta$ $\lambda$ 4102	H $\gamma$ $\lambda$ 4340
4210 – 4230		[O III] $\lambda$ 4363	H $\beta$ $\lambda$ 4861
4400 – 4750 <sup>c</sup>	4400 – 4750 <sup>c</sup>	[O III] $\lambda$ 5007	He I $\lambda$ 5876
5080 – 5100	5150 – 5500		
5600 – 5630			
5970 – 6000		He I $\lambda$ 5876	[N II] $\lambda$ 6549

<sup>a</sup>This window lies on the blue side of the Lyman  $\alpha$  emission line and is only used where no other continuum window is available.

<sup>b</sup>May have some iron emission contamination.

<sup>c</sup>He II  $\lambda$ 4686 lies in this window.

TABLE 3  
INVENTORY OF EMISSION LINES

Emission line	$\lambda_c$ (Å)	FWHM <sup>a</sup> (km s <sup>-1</sup> )	Window <sup>b</sup> (Å)	Notes
Lyman $\beta$ $\lambda$ 1025.7 + O VI $\lambda$ 1035	1030.0	5000	1010 – 1060	See Appendix.
Lyman $\alpha$ $\lambda$ 1215.7	1215.7	7000s 2500n, 8000b	1170 – 1350 ...	
N V $\lambda$ 1241.5	1241.5	6000	...	
O I $\lambda$ 1305	1305.0	2500	...	
Si IV + O IV $\lambda$ 1400	1400.0	5800	1350 – 1450	
C IV $\lambda$ 1549	1549.0	6500s 3000n, 11000b	1350 – 1720 ...	
He II $\lambda$ 1640	1640.0	10000	...	See Appendix.
Al III $\lambda$ 1859	1859.0	3500	1820 – 1970	
C III] $\lambda$ 1909	1909.0	5500	...	
Mg II $\lambda$ 2800	2800.0	4000s 3000n, 8000b	2700 – 2900 ...	Iron emission may be strong in this window.
[Ne V] $\lambda$ 3426	3426.0	1000	3390 – 3460	See Appendix.
[O II] $\lambda$ 3728	3728.0	600	3700 – 3760	See Appendix.
[Ne III] $\lambda$ 3869	3869.0	900	3810 – 3930	See Appendix.
H $\delta$ $\lambda$ 4101.7	4101.7	450	4000 – 4200	
H $\gamma$ $\lambda$ 4340.5 + [O III] $\lambda$ 4363	4352.0	3500	4240 – 4440	
He II $\lambda$ 4686.5	4686.5	1200	4580 – 4790	See Appendix.
H $\beta$ $\lambda$ 4861.3	4861.3	4000s 1000n, 5500b	4750 – 5100 ...	Iron emission may be strong in this window.
[O III] $\lambda$ 4959	4959.0	700	...	Relative strength and separation of [O III] lines is fixed in 1st iteration.
[O III] $\lambda$ 5007	5007.0	600	...	
He I $\lambda$ 5875.6	5875.6	2000	5825 – 5900	

<sup>a</sup>This is the FWHM used for estimating the upper limits of  $W_\lambda$  in weak emission lines. More than one width is given for emission lines that can have two Gaussian components; s = single component, n = narrow component, b = broad component.

<sup>b</sup>The wavelength range over which the emission lines are modeled.

TABLE 4  
TOTAL NUMBER OF EMISSION LINES MODELED

Emission Line	Fixed FWHM and position <sup>a</sup>	$W_\lambda$ upper limits	TOTAL out of 993
UV iron	...	294	953
Optical iron	...	109	247
Lyman $\beta$ + O VI	10	27	130
Lyman $\alpha$	single	2	164
	narrow	0	96
	broad	0	96
N V	24	8	260
O I	20	121	260
Si IV + O IV	12	19	414
C IV	single	3	408
	narrow	0	80
	broad	0	80
He II $\lambda 1640$	66	69	488
Al III	63	181	667
C III]	20	26	667
Mg II	single	3	559
	narrow	0	118
	broad	0	118
[Ne V]	10	365	488
[O II]	27	272	393
[Ne III]	12	259	363
H $\delta$	6	222	309
H $\gamma$ + [O III]	4	87	251
He II $\lambda 4686$	5	155	187
H $\beta$	single	4	141
	narrow	0	7
	broad	0	7
[O III] $\lambda 4959$	6	73	148
[O III] $\lambda 5007$	8	54	148
He I	0	30	33
TOTALS	305	2437	8288

<sup>a</sup>Does not include  $W_\lambda$  upper limits.

TABLE 5  
REPRESENTATIVE EMISSION LINE MEASUREMENTS

Designation	(z)	FWHM	$\Delta\lambda_p$	$W_\lambda$	Absorption
Emission Line		(km s <sup>-1</sup> )	(km s <sup>-1</sup> )	(Å)	Lines
	(1)	(2)	(3)	(4)	(5)
0025+0009	$z = 0.205$				
UV iron		900 <sup>+9000</sup> <sub>-250</sub>	...	70 <sup>+65</sup> <sub>-65</sub>	...
Optical iron		1200 <sup>+8750</sup> <sub>-250</sub>	...	74 <sup>+15</sup> <sub>-15</sub>	...
Mg II	single	2800 <sup>+1000</sup> <sub>-850</sub>	-500 <sup>+440</sup> <sub>-440</sub>	40 <sup>+35</sup> <sub>-30</sub>	...
[Ne V]		1200 <sup>+1100</sup> <sub>-750</sub>	-100 <sup>+380</sup> <sub>-380</sub>	5.5 <sup>+10.0</sup> <sub>-4.3</sub>	...
[O II]		210 <sup>+440</sup> <sub>-200</sub>	100 <sup>+140</sup> <sub>-140</sub>	3.6 <sup>+6.1</sup> <sub>-3.1</sub>	...
[Ne III]		1000 <sup>+3000</sup> <sub>-700</sub>	0 <sup>+2200</sup> <sub>-2200</sub>	5.0 <sup>+30.0</sup> <sub>-4.4</sub>	...
H $\delta$		5500 <sup>+5800</sup> <sub>-1100</sub>	0 <sup>+1100</sup> <sub>-1000</sub>	35 <sup>+55</sup> <sub>-14</sub>	...
H $\gamma$ + [O III]		2800 <sup>+850</sup> <sub>-700</sub>	-200 <sup>+380</sup> <sub>-380</sub>	34 <sup>+20</sup> <sub>-14</sub>	1
He II $\lambda 4686$		1200	...	$\leq 15$	...
H $\beta$	single	3000 <sup>+550</sup> <sub>-500</sub>	300 <sup>+240</sup> <sub>-240</sub>	105 <sup>+35</sup> <sub>-30</sub>	...
[O III] $\lambda 4959$		600 <sup>+1100</sup> <sub>-280</sub>	0 <sup>+550</sup> <sub>-550</sub>	15.0 <sup>+40.0</sup> <sub>-8.5</sub>	...
[O III] $\lambda 5007$		450 <sup>+120</sup> <sub>-120</sub>	100 <sup>+50</sup> <sub>-50</sub>	33 <sup>+13</sup> <sub>-11</sub>	...
He I		600 <sup>+650</sup> <sub>-460</sub>	-300 <sup>+240</sup> <sub>-240</sub>	8.0 <sup>+25.0</sup> <sub>-7.9</sub>	...
2244+0020	$z = 0.973$				
UV iron		4250 <sup>+5750</sup> <sub>-3250</sub>	...	50.6 <sup>+1.7</sup> <sub>-1.7</sub>	...
Al III		6400 <sup>+600</sup> <sub>-500</sub>	900 <sup>+280</sup> <sub>-280</sub>	12.8 <sup>+4.7</sup> <sub>-4.4</sub>	...
C III]		5550 <sup>+180</sup> <sub>-160</sub>	-400 <sup>+90</sup> <sub>-90</sub>	27.9 <sup>+7.3</sup> <sub>-7.2</sub>	...
Mg II	narrow	4000 <sup>+280</sup> <sub>-260</sub>	-250 <sup>+120</sup> <sub>-140</sub>	35.6 <sup>+4.7</sup> <sub>-4.0</sub>	...
	broad	12500 <sup>+2100</sup> <sub>-1500</sub>	200 <sup>+900</sup> <sub>-900</sub>	27.4 <sup>+8.5</sup> <sub>-6.3</sub>	...
[Ne V]		1000	...	$\leq 2.8$	...
2354-0134	$z = 2.211$				
UV iron		2000 <sup>+8000</sup> <sub>-1000</sub>	...	35 <sup>+25</sup> <sub>-25</sub>	...
Lyman $\beta$ + O VI		5400 <sup>+850</sup> <sub>-800</sub>	1300 <sup>+420</sup> <sub>-420</sub>	24.9 <sup>+7.8</sup> <sub>-6.5</sub>	...
Lyman $\alpha$	narrow	3500 <sup>+200</sup> <sub>-200</sub>	150 <sup>+90</sup> <sub>-140</sub>	33 <sup>+11</sup> <sub>-10</sub>	...
	broad	8100 <sup>+440</sup> <sub>-340</sub>	500 <sup>+180</sup> <sub>-240</sub>	57 <sup>+17</sup> <sub>-17</sub>	1
N V		5400 <sup>+400</sup> <sub>-380</sub>	0 <sup>+160</sup> <sub>-220</sub>	34 <sup>+11</sup> <sub>-11</sub>	...
O I		600 <sup>+420</sup> <sub>-440</sub>	100 <sup>+160</sup> <sub>-160</sub>	1.3 <sup>+1.5</sup> <sub>-0.8</sub>	1
Si IV + O IV		5000 <sup>+700</sup> <sub>-650</sub>	0 <sup>+380</sup> <sub>-380</sub>	13.4 <sup>+3.8</sup> <sub>-3.2</sub>	...
C IV	single	6100 <sup>+360</sup> <sub>-360</sub>	50 <sup>+180</sup> <sub>-180</sub>	52.7 <sup>+6.0</sup> <sub>-5.7</sub>	...
He II $\lambda 1640$		17000 <sup>+3800</sup> <sub>-3100</sub>	-1200 <sup>+650</sup> <sub>-650</sub>	26.0 <sup>+12.0</sup> <sub>-8.6</sub>	...
Al III		3500	...	$\leq 7.0$	...
C III]		6500 <sup>+1900</sup> <sub>-1500</sub>	-400 <sup>+900</sup> <sub>-600</sub>	32 <sup>+17</sup> <sub>-12</sub>	...

NOTE.—This is a digested form of the table available from the electronic journal. Only emission lines measured in three example LBQS spectra are presented here, see §4 for more details.

TABLE 6  
REPRESENTATIVE CONTINUUM MEASUREMENTS

Designation (1)	Redshift (2)	$N_H^{\text{Gal}}$ (3)	Power law continua				Polynomial Order (8)
			$\Gamma_1$ (4)	$\lambda_c$ (5)	$A_\lambda$ (6)	$\Gamma_2$ (7)	
0025+0009	0.205	3.010	$3.99^{+1.37}_{-1.51}$	4220	$1.27^{+0.16}_{-0.15}$	$1.08^{+0.48}_{-0.48}$	2
2244+0020	0.973	5.318	$2.50^{+0.01}_{-0.01}$	2170	$15.4^{+0.9}_{-0.1}$	...	2
2354-0134	2.211	3.368	$2.45^{+0.47}_{-0.24}$	1463	$1.19^{+0.04}_{-0.08}$	...	1

NOTE.—This is a digested form of the table available from the electronic journal. Only the continuum parameters from three example LBQS spectra are presented here, see §4 for more details. The units for the normalization of the power law continuum ( $A_\lambda$ ) presented here are  $10^{-16}$  ergs  $\text{cm}^{-2} \text{s}^{-1} \text{\AA}^{-1}$ . In the electronic version of this table the normalization factor is  $10^{-14}$ .

TABLE 7  
EMISSION LINE PARAMETER DISTRIBUTIONS FOR THE LBQS SAMPLE

Emission Line (1)	$W_\lambda$							FWHM		
	Detected			Kaplan-Meier			Num (9)	Mean (10)	Median (11)	
	Num (2)	Mean (3)	SD (4)	Num (5)	Limits (6)	Mean (7)				
UV iron	659	40.2	23.0	953	294	$29.9 \pm 0.8$	27.3	$4610 \pm 130$	3470	
Optical iron	138	39.0	21.5	247	109	$23.8 \pm 1.6$	21.3	$4630 \pm 310$	2600	
Lyman $\beta$ + O VI	103	11.7	10.1	130	27	$9.5 \pm 0.9$	7.3	$4870 \pm 280$	4410	
Lyman $\alpha$	single <sup>a</sup>	164	56.4	28.8	164	$56.4 \pm 2.2$	53.0	162	$7820 \pm 230$	7650
	narrow	96	28.1	21.3	96	$28.1 \pm 2.2$	22.0	96	$2650 \pm 120$	2470
	broad	96	68.3	31.6	96	$68.3 \pm 3.2$	64.0	96	$10250 \pm 420$	9330
	sum <sup>b</sup>	260	71.2	40.4	260	$71.2 \pm 2.5$	61.0	...	...	...
N V	252	18.8	10.7	260	8	$18.3 \pm 0.7$	16.5	228	$5580 \pm 170$	5400
O I	139	3.1	2.5	260	121	$2.0 \pm 0.1$	1.4	119	$2990 \pm 190$	2460
Si IV + O IV	395	13.0	8.8	414	19	$12.6 \pm 0.4$	10.9	383	$6780 \pm 160$	5940
C IV	single <sup>a</sup>	406	38.1	19.3	408	$38.0 \pm 1.0$	34.5	403	$7720 \pm 150$	7300
	narrow	80	17.8	9.3	80	$17.8 \pm 1.0$	15.5	80	$2860 \pm 110$	2750
	broad	80	44.8	23.1	80	$44.8 \pm 2.6$	37.4	80	$10960 \pm 360$	10530
	sum <sup>b</sup>	486	42.1	23.1	488	$42.0 \pm 1.0$	37.0	...	...	...
He II $\lambda 1640$	419	18.7	13.5	488	69	$16.4 \pm 0.6$	12.9	353	$14670 \pm 390$	13590
Al III	486	8.7	6.0	667	181	$6.8 \pm 0.2$	5.2	423	$5740 \pm 130$	5620
C III]	641	28.4	14.9	667	26	$27.6 \pm 0.6$	24.8	621	$7820 \pm 170$	6670
Mg II	single <sup>a</sup>	517	39.1	21.4	559	$37.1 \pm 0.9$	33.8	514	$5160 \pm 120$	4440
	narrow	118	28.1	12.9	118	$28.1 \pm 1.2$	26.0	118	$3510 \pm 110$	3370
	broad	118	36.6	21.5	118	$36.6 \pm 2.0$	31.6	118	$8660 \pm 300$	8880
	sum <sup>b</sup>	635	43.9	25.1	677	$42.0 \pm 1.0$	36.8	...	...	...
[Ne V]	123	5.8	5.8	488	365	$2.1 \pm 0.2$	0.4	113	$1570 \pm 90$	1420
[O II]	121	7.8	14.6	393	272	$3.2 \pm 0.4$	1.0	94	$900 \pm 70$	610
[Ne III]	104	7.5	5.0	363	259	$3.4 \pm 0.2$	1.8	92	$1770 \pm 130$	1380
H $\delta$	87	12.3	8.6	309	222	$3.8 \pm 0.4$	0.1	81	$2860 \pm 220$	2300
H $\gamma$ + [O III]	164	18.3	11.1	251	87	$14.6 \pm 0.7$	11.8	160	$2920 \pm 140$	2500
He II $\lambda 4686$	32	21.0	20.1	187	155	$4.2 \pm 0.9$	0.1	27	$3690 \pm 550$	2350
H $\beta$	single <sup>a</sup>	123	62.4	36.0	141	$57.4 \pm 3.1$	49.8	119	$4370 \pm 250$	3760
	narrow	7	34.3	13.6	7	$34.3 \pm 4.8$	31.4	7	$1160 \pm 270$	900
	broad	7	101.6	58.9	7	$101.6 \pm 0.6$	77.5	7	$6560 \pm 850$	5300
	sum <sup>b</sup>	130	66.4	41.0	148	$61.2 \pm 3.4$	53.8	...	...	...
[O III] $\lambda 4959$	75	13.8	14.0	146	71	$8.5 \pm 1.0$	5.5	69	$940 \pm 80$	770
[O III] $\lambda 5007$	94	30.4	39.0	146	52	$21.6 \pm 2.8$	13.7	86	$820 \pm 70$	590
He I	3	10.7	3.8	33	30	$4.7 \pm 1.1$	1.7	3	$820 \pm 120$	750

<sup>a</sup>The distribution for single Gaussian component models are tabulated separately from narrow and broad components.

<sup>b</sup>The distribution of sum of the broad and narrow component  $W_\lambda$  included with the single component measurements (see §5).

NOTE.—(1) Emission line or line blend. (2) Number of detected emission lines, (3) Mean  $W_\lambda$  of detected emission lines, (4) Standard deviation (SD) of  $W_\lambda$  measurements for detected emission lines. (5) Total number of measured emission lines, (6) The number of upper limits estimates of  $W_\lambda$ , (7)–(8) The KM reconstructed mean and median of the  $W_\lambda$  distributions (see §5). (9)–(11) The number, mean and median of the distribution of FWHM of the Gaussian components used to model each emission feature. All  $W_\lambda$  are rest frame measurements in Å and the FWHM are in km s<sup>-1</sup>.

TABLE 8  
EMISSION LINE PARAMETER DISTRIBUTIONS FOR PUBLISHED COMPARISON SAMPLES

Emission Line (1)	Ref (2)	Num (3)	Limits (4)	$W_\lambda$ Mean (5)	Median (6)	Num (7)	FWHM Mean (8)	FWHM Median (9)	
UV iron	2	38	8	$28.1 \pm 4.8^a$	21.5	...	...	...	
Optical iron	1	87	7	$47.5 \pm 2.8$	43.8	...	...	...	
	2	45	5	$178.5 \pm 6.2$	110.9	...	...	...	
3Q	14	...	...	$25.6 \pm 4.9$	...	...	...	...	
3L	17	...	...	$34.4 \pm 4.2$	...	...	...	...	
4Q	80	...	...	$52 \pm 2.8^b$	...	...	...	...	
	4L	45	...	$21.5 \pm 2.5^b$	...	...	...	...	
Lyman $\alpha$	3Q	11	...	$72.2 \pm 9.0$	...	...	...	...	
	3L	6	...	$99.2 \pm 9.0$	...	...	...	...	
C IV	single	3Q	13	...	$22.6 \pm 3.4$	...	15	$4880 \pm 460$	
		3L	13	...	$20.0 \pm 2.5$	...	15	$6020 \pm 670$	
narrow	2	39	0	$11.2 \pm 1.4$	8.7	39	$1560 \pm 80$	1560	
broad	2	52	0	$107.5 \pm 9.4$	96.0	51	$6990 \pm 310$	6610	
He II $\lambda 1640$	2	44	3	$25.3 \pm 2.7$	23.4	24	$12940 \pm 600$	12400	
C III] $\lambda 1909$	3Q	10	...	$17.9 \pm 1.6$	...	12	$6430 \pm 730$	...	
	3L	13	...	$17.9 \pm 0.7$	...	14	$8420 \pm 620$	...	
Mg II $\lambda 2800$	3Q	7	...	$23.1 \pm 2.3$	...	...	...	...	
	3L	6	...	$29.1 \pm 4.1$	...	...	...	...	
He II $\lambda 4686$	1	70	0	$11.2 \pm 1.1$	7.5	...	...	...	
	2	32	5	$16.8 \pm 2.4$	13.5	14	$7480 \pm 770$	7900	
H $\beta$	single	1	87	0	$95.5 \pm 4.0$	92.5	87	$3790 \pm 220$	3160
	3Q	14	...	$64.8 \pm 6.9$	...	14	$4430 \pm 590$	...	
	3L	17	...	$73.2 \pm 5.1$	...	17	$5100 \pm 470$	...	
	4Q	80	...	$99 \pm 4.2^b$	...	...	...	...	
	4L	45	...	$84 \pm 5.2^b$	...	...	...	...	
narrow	2	42	0	$4.9 \pm 0.6$	4.0	38	$630 \pm 40$	590	
broad	2	52	0	$105.3 \pm 8.4$	107.0	51	$5950 \pm 550$	4780	
	3Q	...	...	...	...	14	$9870 \pm 970$	...	
	3L	...	...	...	...	17	$11890 \pm 600$	...	
[O III] $\lambda 5007$	1	83	0	$24.8 \pm 2.7$	16.8	...	...	...	
	2	49	0	$58.8 \pm 6.8$	23.4	49	$700 \pm 40$	610	
	3Q	15	...	$20.6 \pm 3.5$	...	14	$1160 \pm 90$	...	
	3L	17	...	$10.2 \pm 1.9$	...	15	$1150 \pm 130$	...	
	4Q	80	...	$23.5 \pm 2.9^b$	...	...	...	...	
	4L	45	...	$23.0 \pm 2.2^b$	...	...	...	...	

<sup>a</sup>This measurement is not suitable for direct comparison with the mean from the LBQS sample (Table 8) because it is measured in a different region of the spectrum (see §6).

<sup>b</sup>Errors on mean calculated from  $\sigma/\sqrt{N}$ .

NOTE.—(1) Emission line or line blend. (2) Reference. (3) The total number of measured emission lines, (4) Number of upper limits on  $W_\lambda$ . (5)–(6) The mean and median of the  $W_\lambda$  distributions. Where upper limits are present the KM estimator was used (see §5). (7)–(9) The number, mean and median of the distribution of published FWHM. All  $W_\lambda$  are rest frame measurements in Å and the FWHM are in km s<sup>-1</sup>.

REFERENCES.—(1) Boroson & Green 1992; (2) Marziani et al. 1996; (3) McIntosh et al. 1999; (4) Sulentic et al. (2000); Q = Radio Quiet, L = Radio Loud

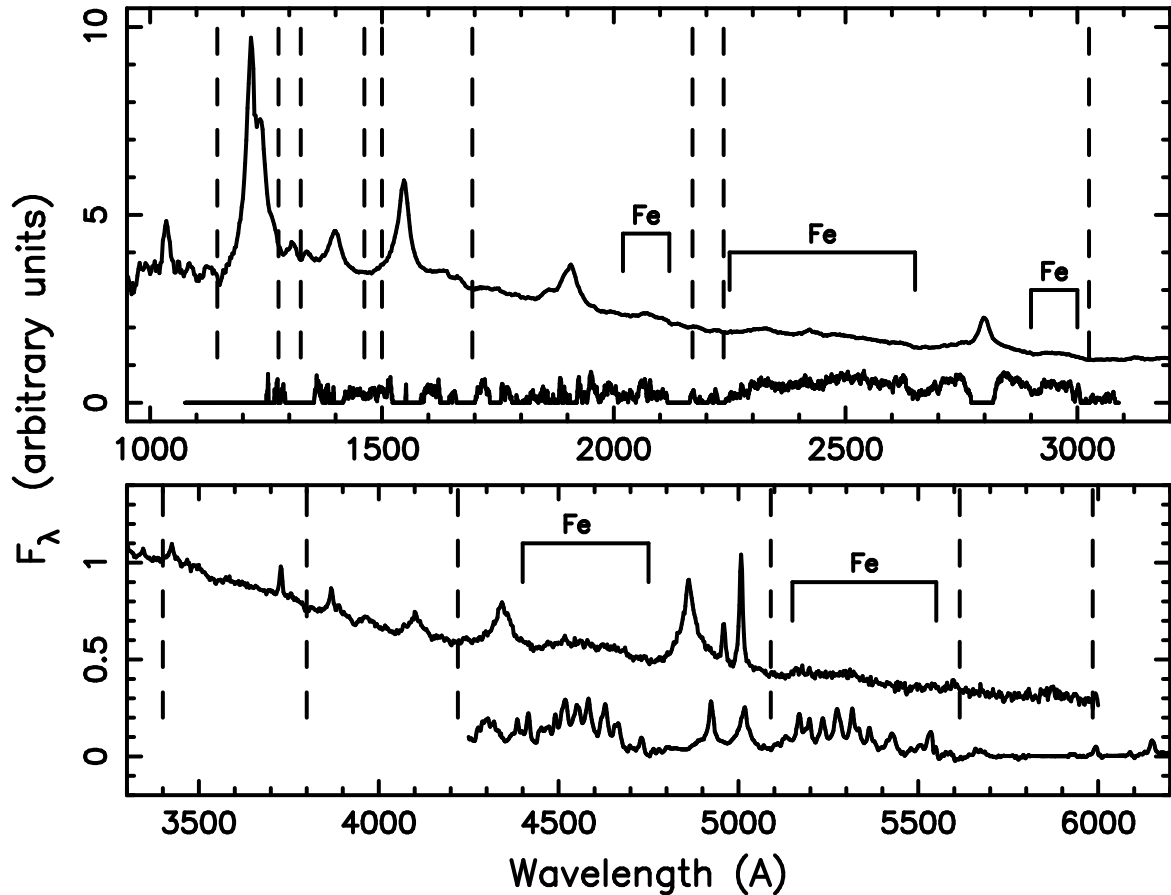


Fig. 1.— Continuum and iron template modeling windows. The composite QSO spectrum from Francis et al. (1991) is shown above the iron emission templates for the UV (upper panel) and optical (lower panel) regions. The vertical dashed lines mark the positions of the narrow windows used to constrain the continuum shape for each spectrum. The spectral windows used in the modeling of iron emission are shown. See §§3.1, 3.2 and Table 2 for further details.

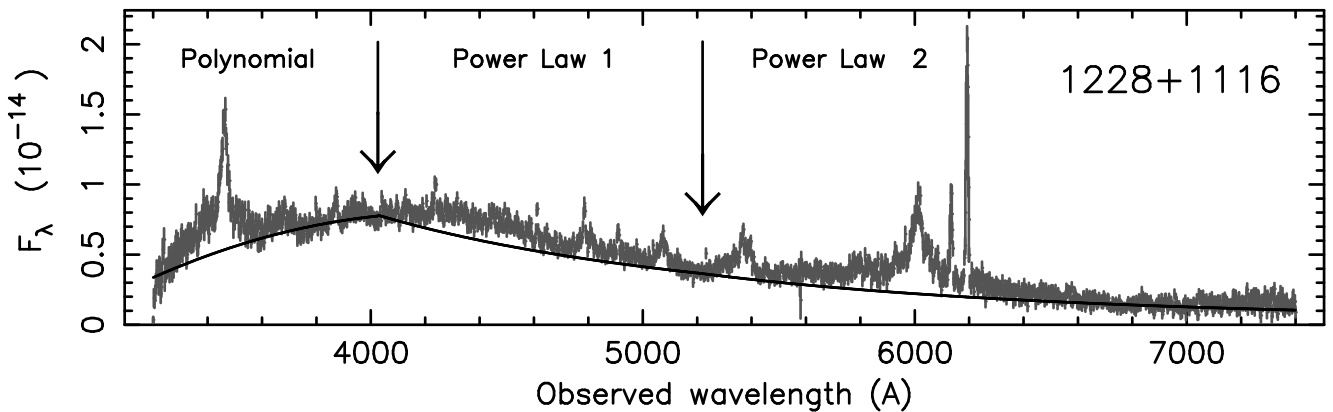


Fig. 2.— The continuum model for LBQS 1228+1116 ( $z=0.237$ ). The bond between the polynomial continuum and the first power law is at  $4000\text{Å}$  in the *observed* frame and the inflection point between the two power law continua is at *rest frame*  $4220\text{Å}$  (see §3.1).

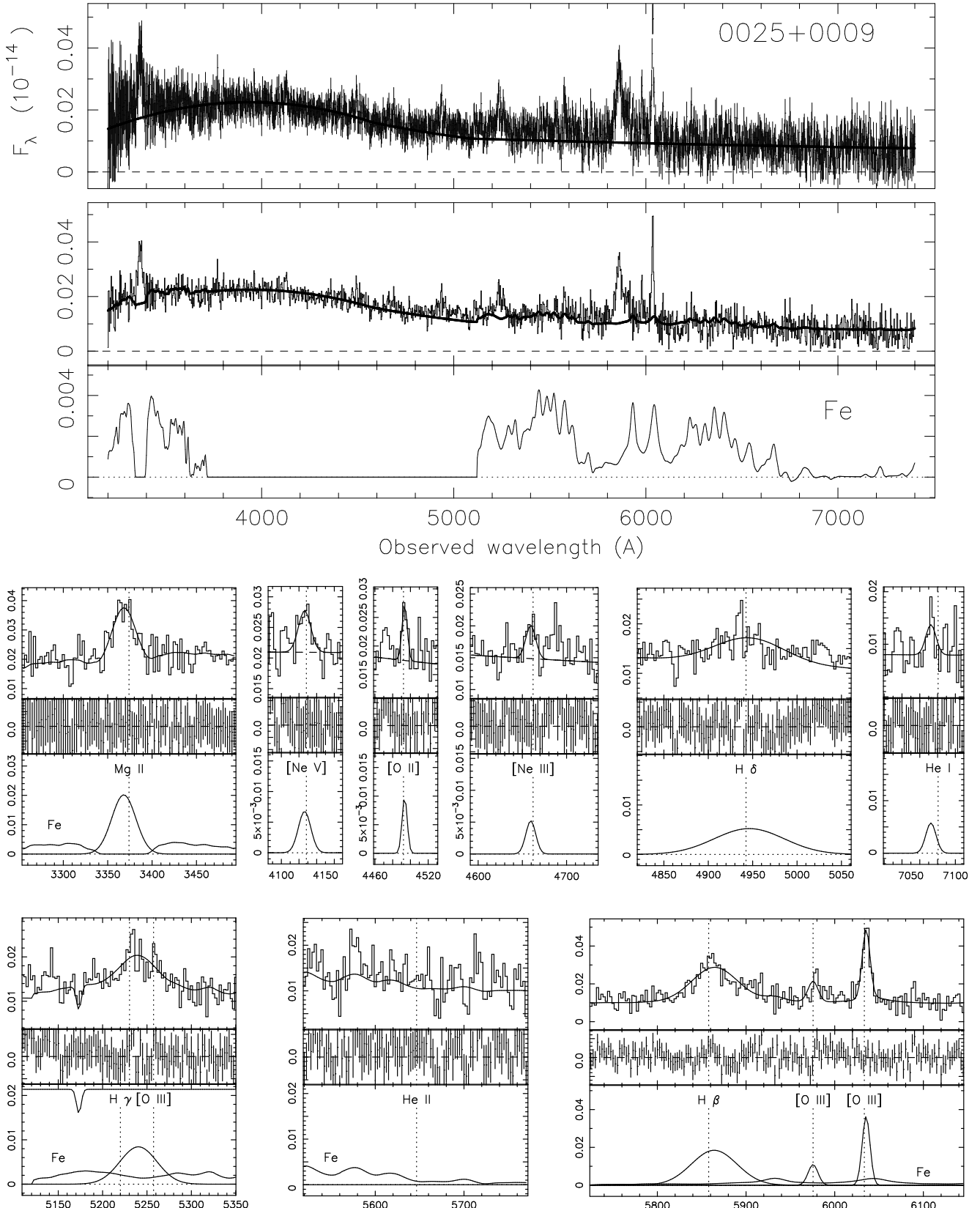


Fig. 3a.— The spectral models of three QSOs from the LBQS sample. For each QSO, the top panel shows 3 sections. The continuum model plotted over the observed spectrum including error bars on each bin, the continuum + iron emission template plotted over the spectrum, and the iron template profile alone. Note that for clarity the flux scales are different in these sections. Smaller panels for each emission line component show the total best-fit model plotted over the relevant region of each spectrum, the residuals, and the individual Gaussian components (and the profile of the iron template emission). Flux units are  $10^{-14}$  ergs  $\text{cm}^{-2}\text{s}^{-1}\text{\AA}^{-1}$ , wavelength units are in  $\text{\AA}$  and are observed frame values. Broad and narrow components of the same emission line species are marked ‘b’ or ‘n’ respectively. See §4 for more details. (a) — The spectral model of LBQS 0025+0009.

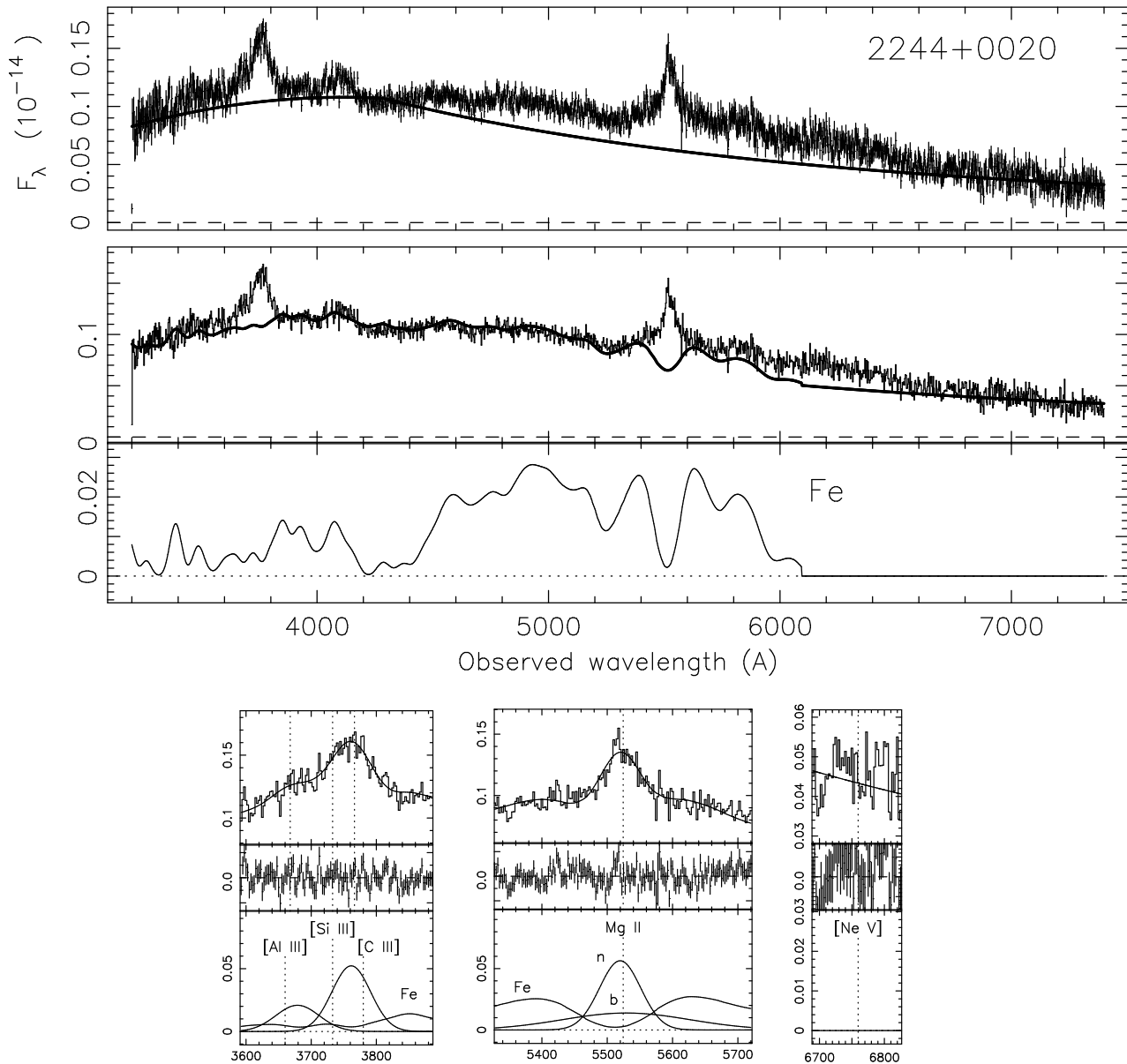


Fig. 3b.— The spectral model of LBQS 2244+0020 — See Fig.3a and §4.

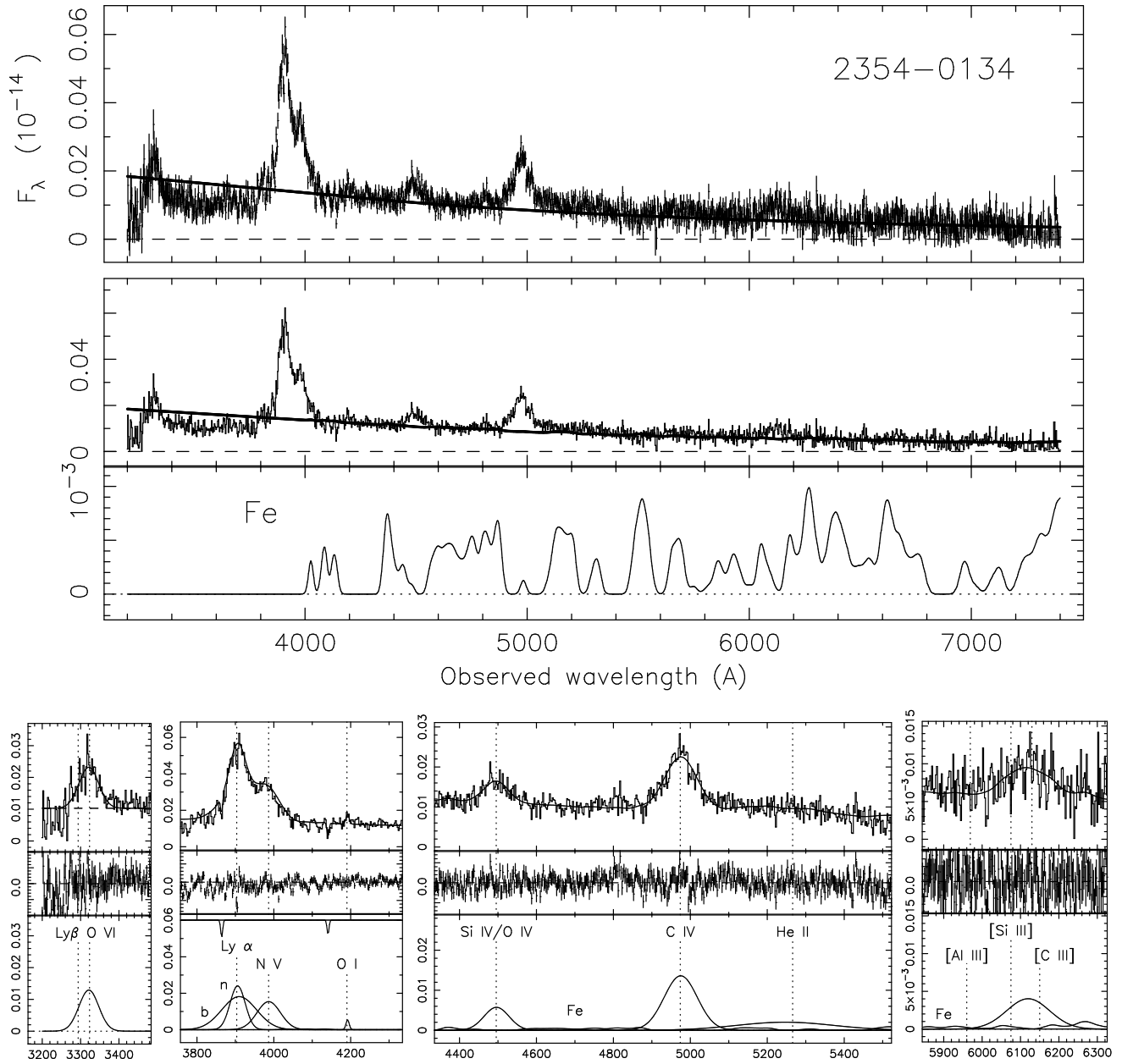


Fig. 3c.— The spectral model of LBQS 2354–0134 — See Fig.3a and §4.

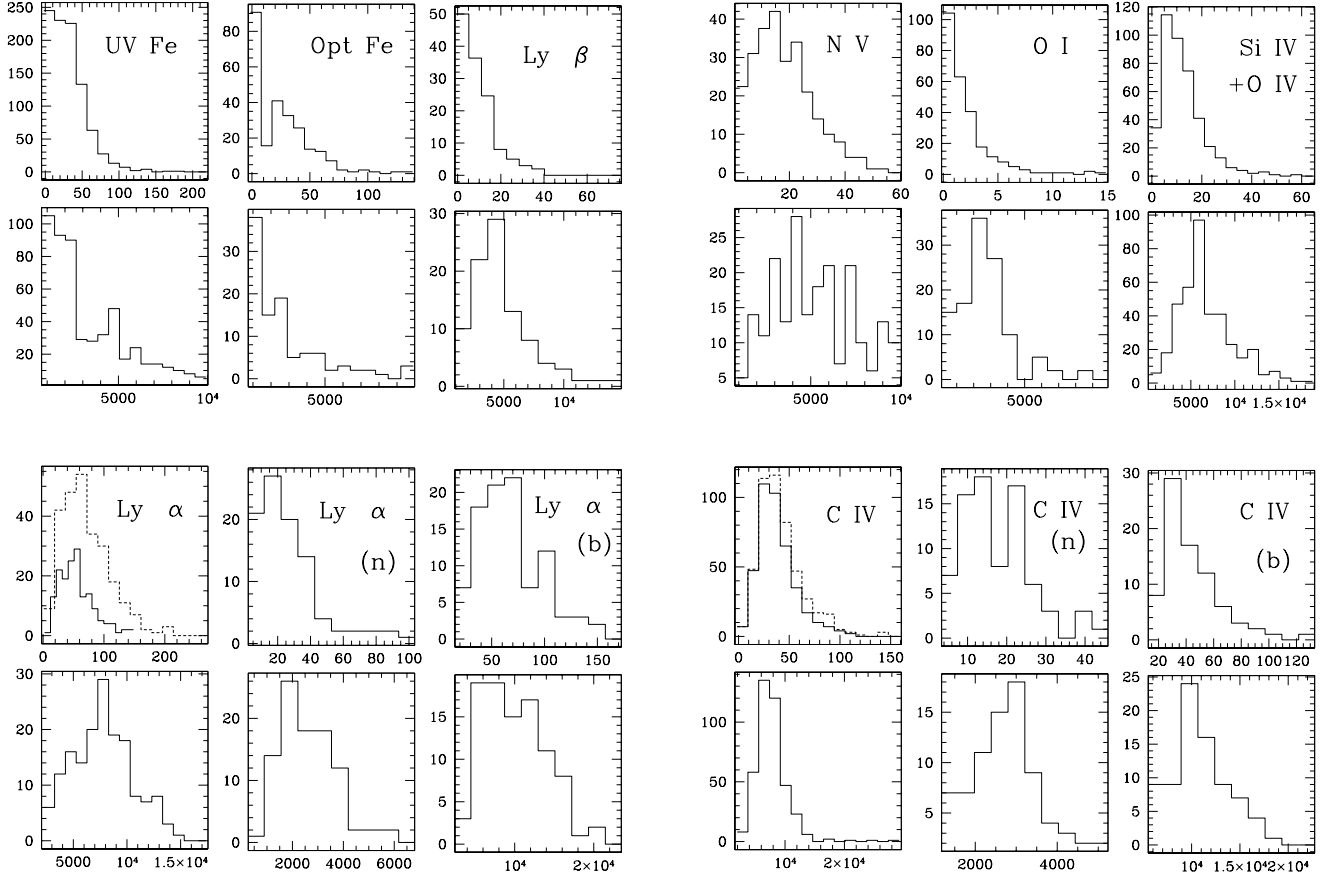


Fig. 4.— The KM estimated distribution of the emission line properties of the LBQS sample. The upper panels are rest frame  $W_\lambda$  (Å) and the lower panels are the FWHM (km s $^{-1}$ ) of the Gaussian profile used to model the emission lines (see §3.2 and §4 for an explanation of the meaning of the iron emission  $W_\lambda$  and FWHM). For emission lines that may be modeled with two Gaussian profiles, the narrow component distributions are marked (n) and broad components (b). The distribution of the sum of the narrow + broad component  $W_\lambda$  is also shown as the dashed line in the panels for the single component models.

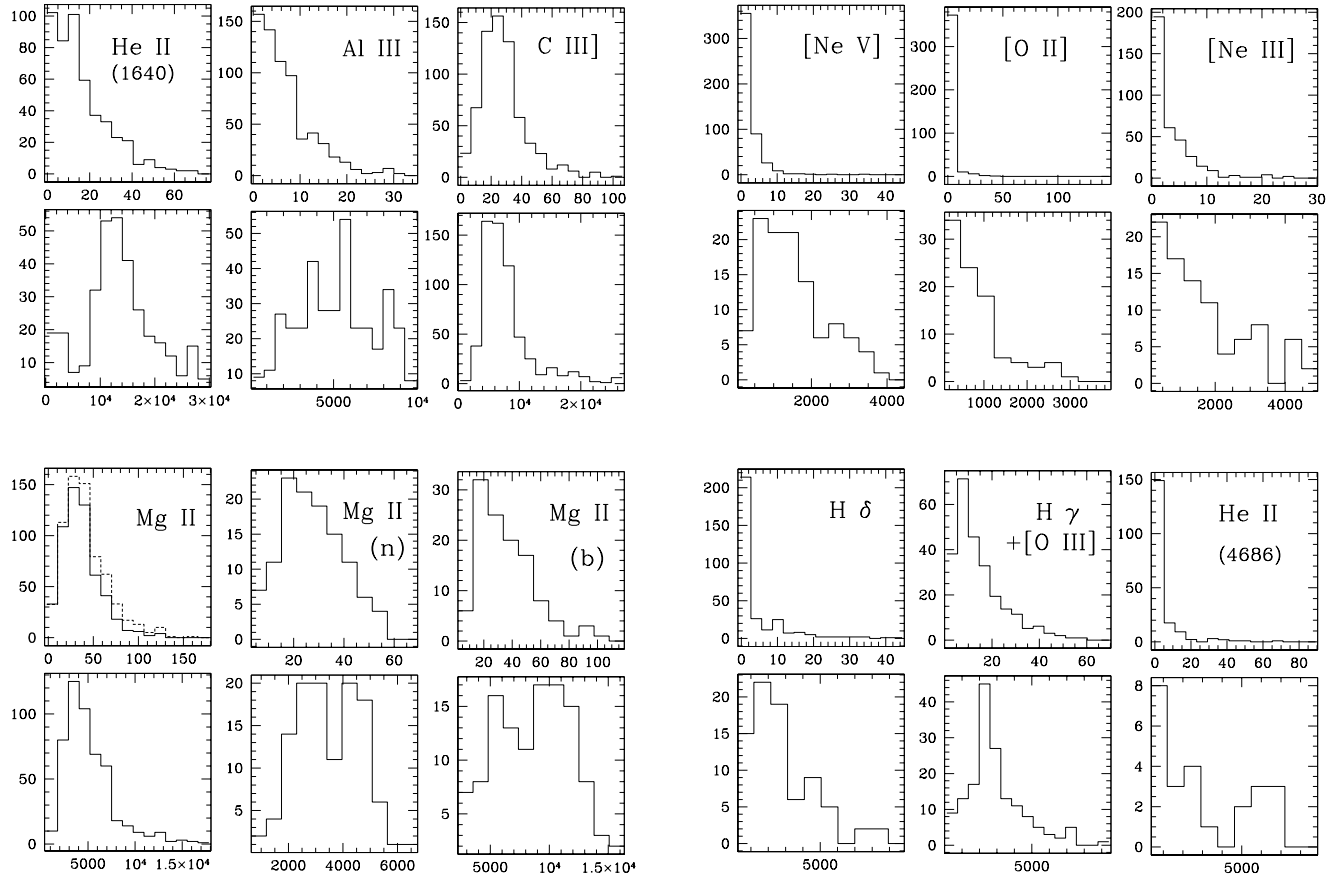


Fig. 4.—Cont.

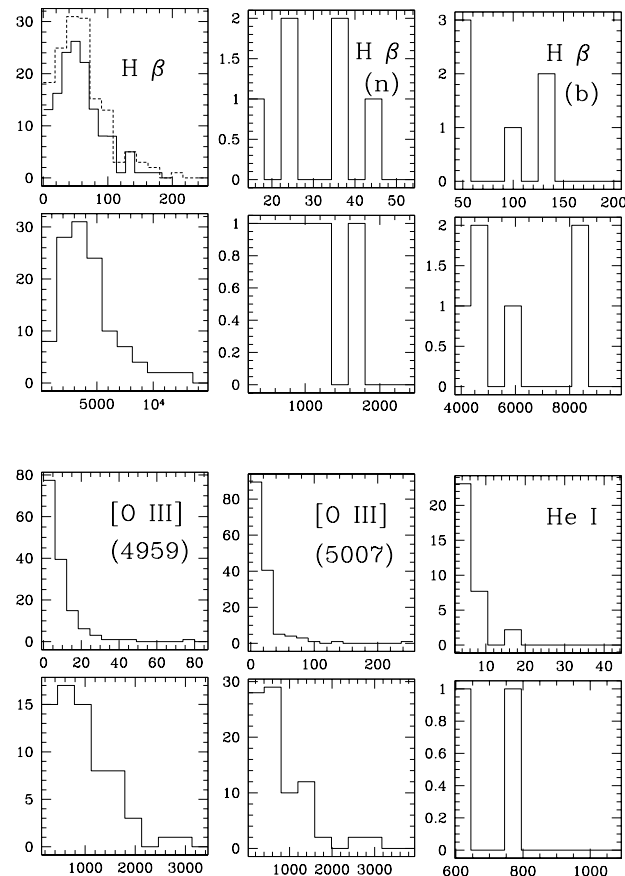


Fig. 4.— Cont.